ผลกระทบของการเดินเส้นโลหะสองชั้นต่อสมรรถนะของตัวรับรู้ซิลิกอนแบบแถบ

นางสาวนันทา โสภณรัตน์

วิทยานิพนธ์นี้เป็นส่วนหนึ่งของการศึกษาตามหลักสูตรปริญญาวิทยาศาสตรมหาบัณฑิต
สาขาวิชาฟิสิกส์ ภาควิชาฟิสิกส์
คณะวิทยาศาสตร์ จุฬาลงกรณ์มหาวิทยาลัย
ปีการศึกษา 2556

IMPACT OF DOUBLE-LAYER METAL ROUTING ON SILICON STRIP SENSOR PERFORMANCE

Ms. Nanta Sophonrat

A Thesis Submitted in Partial Fulfillment of the Requirements
for the Degree of Master of Science Program in Physics
Department of Physics
Faculty of Science
Chulalongkorn University
Academic Year 2013

Thesis Title	IMPACT OF DOUBLE-LAYER METAL ROUTING ON SILICON STRIP SENSOR PERFORMANCE
By	Ms. Nanta Sophonrat
Field of Study	Physics
Thesis Advisor	Assistant Professor Burin Asavapibhop, Ph.D.
Thesis Co-Advisor	Professor Meenakshi Narain, Ph.D. Alexandra Junkes, Ph.D.

Accepted by the Faculty of Science, Chulalongkorn University in Partial Fulfillment of the Requirements for the Master's Degree

.... Dean of the Faculty of Science
(Professor Supot Hannongbua, Dr.rer.nat.)

THESIS COMMITTEE

.... Chairman
(Assistant Professor Rattachat Mongkolnavin, Ph.D.)

.... Thesis Advisor
(Assistant Professor Burin Asavapibhop, Ph.D.)

.... Thesis Co-Advisor
(Professor Meenakshi Narain, Ph.D.)

.... Thesis Co-Advisor
(Alexandra Junkes, Ph.D.)

.... Examiner
(Assistant Professor Somchai Kiatgamolchai, Ph.D.)

.... External Examiner
(Assistant Professor Udomrat Tippawan, Ph.D.)

นันทา โสภณรัตน์ : ผลกระทบของการเดินเส้นโลหะสองชั้นต่อสมรรถนะของตัวรับรู้ซิลิกอนแบบแถบ (IMPACT OF DOUBLE-LAYER METAL ROUTING ON SILICON STRIP SENSOR PERFORMANCE). อ.ที่ปรึกษาวิทยานิพนธ์หลัก : ผศ.ดร.บุรินทร์ อัศวพิภพ, อ.ที่ปรึกษาวิทยานิพนธ์ร่วม : PROF. MEENAKSHI NARAIN, Ph.D., ALEXANDRA JUNKES, Ph.D., 70 หน้า.

ในปี 2020 เครื่องตรวจจับอนุภาคซีเอ็มเอส จะต้องรับมือกับระดับรังสีที่เพิ่มสูงขึ้นจากเครื่องชนอนุภาคขนาดใหญ่ (แอลเอชซี) ที่ถูกปรับปรุงให้มีค่าลูมินอซิตีในระดับสูง ส่วนตรวจหารอยทางเดินอนุภาคของซีเอ็มเอส จะต้องถูกปรับปรุงเพื่อให้มีความทนทานต่อรังสีมากขึ้นและเพื่อลดปริมาณวัสดุที่ใช้ ในงานนี้ เราได้ทำการทดสอบตัวรับรู้ซิลิกอนแบบแถบของซีเอ็มเอส รูปแบบใหม่ที่เป็นทางเลือก ซึ่งได้รวมส่วนของตัวปรับความกว้างระหว่างเส้นไว้ในตัวมันโดยอาศัยการเดินเส้นโลหะสองชั้น ตัวปรับความกว้างระหว่างเส้นซึ่งทำจากแก้วที่มีการเดินเส้นโลหะอยู่ด้านบนนั้น ใช้เป็นส่วนเชื่อมต่อระหว่างตัวรับรู้และชิพที่ใช้อ่านข้อมูล การรวมตัวปรับความกว้างระหว่างเส้นเข้าไว้ในตัวรับรู้ ช่วยลดปริมาณวัสดุที่ใช้ในส่วนตรวจหารอยทางเดินอนุภาคของซีเอ็มเอส และทำให้การออกแบบตัวรับรู้ขนาดเล็กมีความยืดหยุ่นมากขึ้น ตัวรับรู้ที่ใช้ทดสอบในงานนี้เป็นส่วนหนึ่งของโครงการเอชพีเคของหน่วยงานที่ดูแลส่วนตรวจหารอยทางเดินอนุภาคของซีเอ็มเอส บนตัวรับรู้นั้น มีทั้งบริเวณที่มีและไม่มีการเดินเส้นโลหะสองชั้น และบริเวณที่มีความยาวของการเดินเส้นโลหะสองชั้นแตกต่างกัน เราได้ทำการศึกษาผลของการเดินเส้นโลหะสองชั้นต่อการรวบรวมประจุและค่าสัญญาณต่อการรบกวน ส่วนของการทดลองนั้น ได้ดำเนินการที่มหาวิทยาลัยบราวน์ การทดสอบคุณภาพของตัวรับรู้ที่ใช้ทดสอบทำได้โดยการวัดคุณสมบัติทางไฟฟ้า เราได้ทำการวัดสัญญาณจากตัวรับรู้ก่อนและหลังการฉายรังสีด้วยอนุภาคโปรตอนที่มีพลังงาน 800 เมกะอิเล็กตรอนโวล์ต โดยฟลูเอนซ์เทียบได้กับค่าจากแอลเอชซีที่ปรับปรุงแล้ว ไม่พบความแตกต่างของการรวบรวมประจุและค่าสัญญาณต่อการรบกวนที่มีนัยสำคัญระหว่างบริเวณต่างๆ การแบ่งประจุระหว่างแถบที่ติดกันสองแถบ(แถบหนึ่งมีการเดินเส้นโลหะสองชั้นและอีกแถบหนึ่งไม่มี) ได้ช่วยเสริมข้อสรุปนี้

ภาควิชา ฟิสิกส์ ลายมือชื่อนิสิต ....
สาขาวิชา ฟิสิกส์ ลายมือชื่อ อ.ที่ปรึกษาวิทยานิพนธ์หลัก ....
ปีการศึกษา 2556 ลายมือชื่อ อ.ที่ปรึกษาวิทยานิพนธ์ร่วม..........................
ลายมือชื่อ อ.ที่ปรึกษาวิทยานิพนธ์ร่วม..........................

5572017423 : MAJOR PHYSICS
KEYWORDS : CMS SILICON STRIP SENSOR, DOUBLE METAL ROUTING, CHARGE COLLECTION, SIGNAL TO NOISE RATIO, CHARGE SHARING

NANTA SOPHONRAT : IMPACT OF DOUBLE-LAYER METAL ROUTING ON SILICON STRIP SENSOR PERFORMANCE. ADVISOR : ASST. PROF. BURIN ASAVAPIBHOP, Ph.D., CO-ADVISOR : PROF. MEENAKSHI NARAIN, Ph.D., ALEXANDRA JUNKES, Ph.D., 70 pp.

In 2020, the CMS detector will suffer from higher radiation dose of the upgraded High-Luminosity LHC. The CMS Tracker has to be upgraded to be radiation harder and to reduce its material budget. In this work, new optional design of the CMS silicon strip sensor is tested, where the Pitch Adapter (PA) was integrated into the sensor's structure via the second-metal-layer routing. The PA, which is made of glass with metal routing on top, is used as an interface between the silicon strip sensor and the readout chip. Incorporating the PA to the sensor helps reducing the material budget of the CMS Tracker and allows a flexible design of a smaller sensor. The test sensors are parts of the HPK campaign of the CMS Tracker collaboration. There are regions on the sensors with and without double metal (DM) routing, and regions with different double metal routing lengths. The effects of the double-layer metal routing on charge collection and signal to noise ratio (S/N) are investigated in this work. The experimental parts were done at Brown University. The quality of the test sensors were checked by electrical properties measurements. The signal measurements were made before and after irradiation with 800-MeV proton, to the fluence comparable to that of the upgraded LHC. No significant difference on charge collection and S/N between different regions were observed. The charge sharing between two consecutive strips (one strip with DM and other strip without DM) further confirms this conclusion.

Department : Physics .... Student's Signature ....
Field of Study : Physics .... Advisor's Signature ....
Academic Year : 2013 .... Co-Advisor's Signature ....
Co-Advisor's Signature ....

Acknowledgements

I would like to express my sincere gratitude to my supervisors at Brown University, Prof. Meenakshi Narain, Prof. Ulrich Heintz, and Dr. Alexandra Junkes for their helps and insightful suggestions. I would also like to express my sincere gratitude to my supervisor, Asst. Prof. Dr. Burin Asavapibhop, for his kind suggestions and valuable supports. I am deeply thankful to Alex Garabedian, Sinan Sagir, and David Tersegno, the members of Brown Experimetal Particle Physics laboratory, for their helps on the experiments, all of the valuable suggestions, and being kind and helpful to me all the time. I would also like to thank Zaixing Mao for letting me adapt his analysis code. I would also like to thank the members of Particle Physics Research laboratory at Chulalongkorn University, Dr.Narumon Suwonjandee, Dr.Norraphat Srimanobhas, and Dr. Emanuele Simili for their kind comments and suggestions. Without all of them this thesis would not be complete.

I am very thankful for having a great support and understanding from my family. Nothing would mean anything without them. I would also like to thank all of my friends in Chulalongkorn University for their welcome and accompany, for making my time in this University meaningful.

I would like to thank the Development and Promotion of Science and Technology Talents Project (DPST) for supporting my education since high school. This thesis is supported partially by the Special Task Force for Activating Research Project (STAR), Ratchadaphiseksomphot Endowment Fund, Chulalongkorn University.

Contents

List of Tables

List of Figures

Figure **page**

Figure **page**

Figure **page**

Figure **page**

CHAPTER I

INTRODUCTION

In this work, the sensor with integrated pitch adapter on the second metal layer, known as Double Metal (DM) sensor, is studied. Brief introductions on the LHC, CMS detector and CMS tracker, are presented in section 1.1 - 1.3 as a background knowledge for developing the motivations for the Double Metal sensor in the last section. The theorical backgrounds for silicon detector are presented in chapter 2. Designs of the test sensors, reviews of previous works, and expected behaviors are discussed in chapter 3. The qualification of the test sensors were done by electrical properties measurement which is presented in chapter 4. In chapter 5, methods and results of signal measurements which were done before and after irradiation are discussed.

1.1 The LHC

The Large Hadron Collider (LHC) is a 27-km-circumference circular particle accelerator and collider located in the tunnel 100 m under the Swiss-France border at Geneva. It is the lastest, biggest and highest energy ring of the CERN accelerator complex which is composed of chains of linear and circular accelerators. Inside the LHC ring, there are two separated rings that accelerate bunches of protons in the opposite direction. The intersections of these two rings are the points where the two proton beams collide and new particles are created from the conversion of energy into mass. There are four collision points along the LHC ring and each point is covered by a giant detector. These detectors have different designs based on their goals of studies. The four detectors are: A Toroidal LHC Apparatus (ATLAS), Compact Muon Solenoid (CMS), A Large Ion Collider Experiment (ALICE), and Large Hadron Collider beauty (LHCb).

ATLAS and CMS have the main purpose of finding Higgs bosons. Although

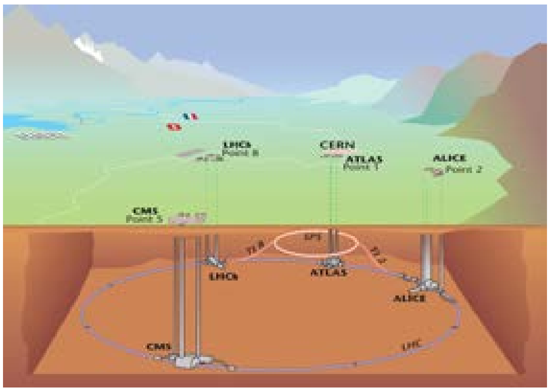

Figure 1.1: The LHC lies 100 m under the border of Switzerland and France. The connections to the ground are at ATLAS, CMS, ALICE and LHCb experiments[1].

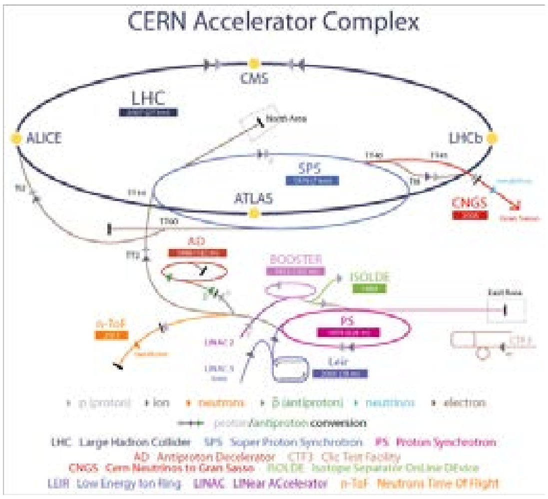

Figure 1.2: The chain of accelerators ranges from LINAC to LHC[2].

they have already confirmed the discovery of the Higgs boson at the beginning of 2013, they still have a lot of works to do engaging all the beyond standard model theories that predict e.g. Higgs' brothers and sisters, dark matter candidates, and magnetic monopoles.

ALICE focuses on the study of the conditions of the early universe after the big bang where the particles are in a very high temperature and density conditions: the state of quark-gluon plasma. This phase is expected in the collision of high energy lead nuclei.

LHCb studies why there is an asymmetry of number of particles and antiparticles in the Universe by studying the interactions involving B mesons.

The LHC was designed to collide two beams of proton with the center of mass energy of 14 TeV and the luminosity of 5×10^{34} cm^{-2}s^{-1} . This can be done by gradually increase the energy and luminosity through the series of upgrade [1].

- In 2012, the LHC was running with center of mass energy of 8 TeV and the luminosity of $\sim 10^{32}$ cm^{-2}s^{-1}.
- The Long Shutdown 1 (LS1), 2013 - 2014, is to prepare the LHC to operate at 14 TeV with the luminosity of $\sim 10^{33} - 10^{34}$ in late 2014 - 2016 run.

---

[1] Figure from: http://www.atlas.ch/photos/lhc.html

[2] Figure from: http://www.quantumdiaries.org/2011/04/24/the-cern-accelerator-complex/

- The Long Shutdown 2 (LS2) in 2017 will prepare the LHC to run at 14 TeV with high luminosity (5×10^{34} cm^{-2}s^{-1}) in 2018 - 2020.

During the LHC shutdowns, each detector will be upgraded and prepared for the next run.

1.2 CMS Detector

Compact Muon Solenoid (CMS) detector[3] consists of layers of different-function detectors based on what properties to measure. The order of the layers is importance e.g. electron and photon have a higher energy-loss rate than hadrons, therefore the layer for measuring energy of electron and photon should come before that of hadrons. Fig.1.3 shows different layers of CMS detector. The components from the inside to the outside are:

- Silicon Tracker: reconstructing tracks of charged particles
- Electromagnetic calorimeter: measuring energy of electrons and photons by means of scintillation
- Hadron calorimeter: a sampling calorimeter which measures energy and locates hits of hadrons e.g. protons, neutrons, pions, kaons
- Superconducting solenoid: bending the paths of the charged particles, therefore we can distinguish type of charge and caluculate monemta
- Muon chamber: detecting muons

In this thesis, we will focuese on the Silicon Tracker only.

1.3 CMS Tracker

CMS Tracker is composed of 1,440 pixel modules and 15,148 silicon strip modules [2]. Fig.1.4 shows its 2D layout with respect to the collision point in the CMS detector. The black dot represents the collision point. The innermost part is the pixel detector with 3 barrel layers and 2 end cap disks on each side. The size of the

---

[3] Find out more at CMS website: http://cms.web.cern.ch/news/what-cms

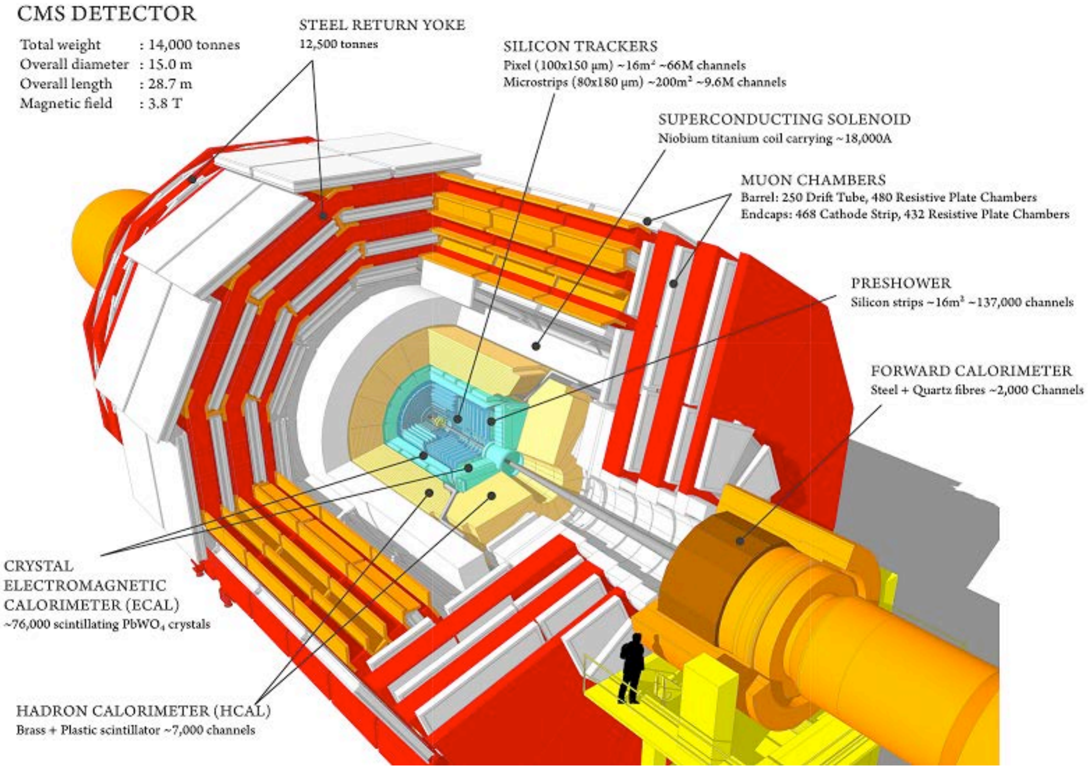

Figure 1.3: The components of the CMS detector[4].

pixel detector barrel is 20 cm in diameter and 55 cm long. All other parts belong to the silicon strip detector which is composed of 4 Tracker Inner Barrel layers (TIB) with intermediate radii of 20 cm to 55 cm, 3 layers of forward Tracker Inner Disk(TID), 6 barrel layers of Tracker Outer Barrels (TOB), and 9 layers of Tracker End Caps (TEC). Each line represents a CMS detector module. The double line represents double-side module used to provide 2D position. Fig. 1.5 displays parts of a silicon strip module which consists mainly of silicon strip sensors (one or two sensors depend on the position in the Tracker), a pitch adapter, a front-end hybrid, and supporting structures. The pitch of the sensor, the distance between two strips, is one of the key parameters in designing the strip sensor to obtain a good resolution while having a good signal separation between each strip. The pitches of the sensors on different layers are not equal. They are in the range of 80 to 184 μm [2]. However, the pitch of the readout chip on the front-end hybrid is fixed at 44 μm. Therefore, pitch adapters with different configurations are used as the interfaces. They are made of aluminum routing on top of glass substrate [3].

---

[4] Figure from: http://cms.web.cern.ch/news/cms-detector-design

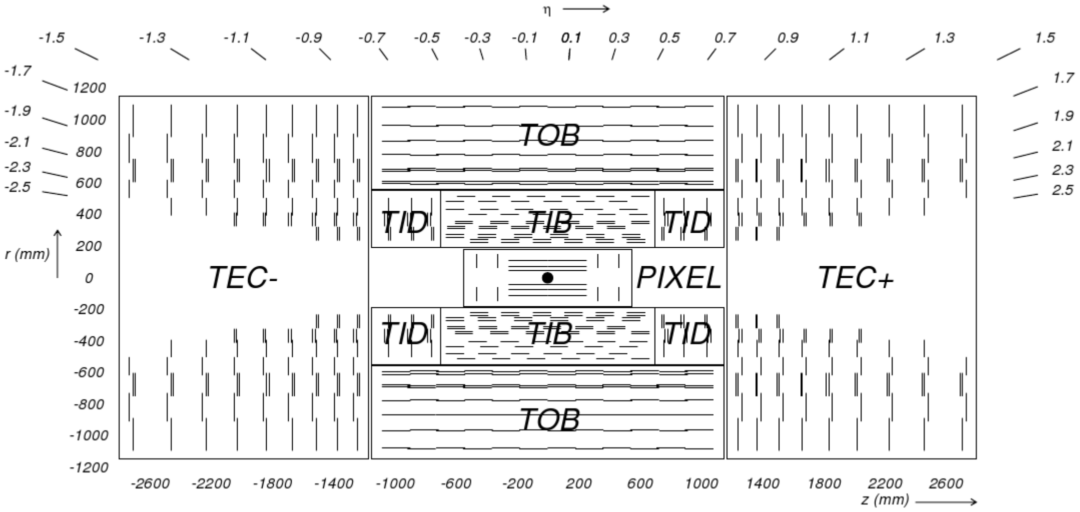

Figure 1.4: Longitudianl cross section of CMS Tracker shows the layout of detector modules[5][2].

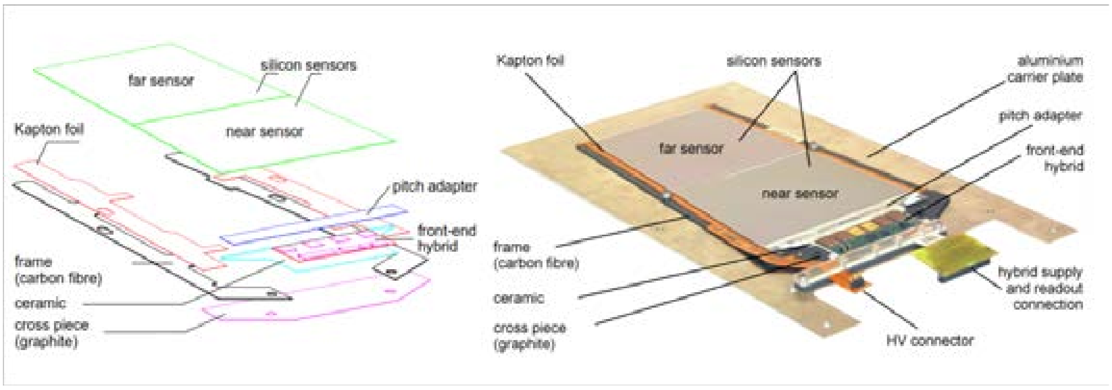

Figure 1.5: Components of CMS TOB module: silicon strip sensors, pitch adapter, front-end hybrid, and supporting frame. The strips of the two sensors are connected one-to-one [2].

1.4 Motivation for Double Metal

As stated earlier, the pitch of the silicon strip sensor is not equal to the pitch of the readout chip. Therefore, the Pitch Adapter (PA) is necessary for the interface between the two. In this work, we investigate the double metal sensor that integrates the PA onto the top of the present silicon sensor by adding the second

---

[5] For the definition of pseudorapidity, η, see Appendix A.2: CMS detector coordinate.

metal routing layer. The motivations for this effort are to reduce the material budget and to help in designing new smaller sensor to increase the granularity of the CMS detector.

1.4.1 Reducing Material Budget

Every time two bunches of proton collide at the center of the CMS detector, new particles are created from the conversion of energy into mass. Most of these new particles are short-lived and will decay into more stable particles which we can detect e.g. electrons, muons, protons, pions, and kaons. As these particles travel out of the interaction point, they pass through various components of the CMS detector including sensors, electronics, cables, cooling pipes, and supporting structures. Because the particles pass through the Tracker before reaching the Electromagnetic Calorimeters, some of their energies are deposited on the Tracker. Therefore, before running the experiment, a study must be conducted to figure out how much energy is deposited on the Tracker. This is known as the material budget of the detector.

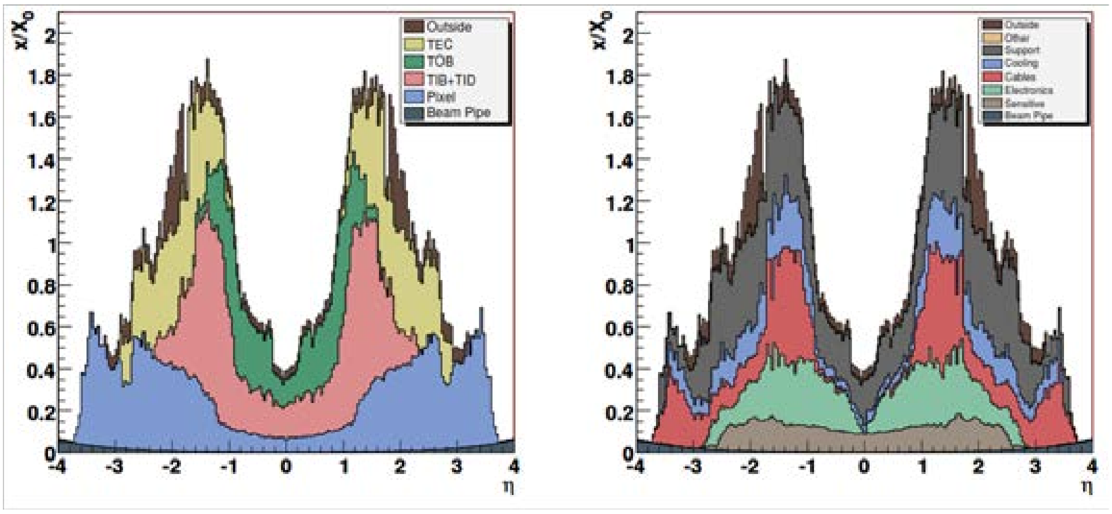

Figure 1.6: Simulated material budget of CMS Tracker in the units of radiation length classified by detector modules (left) and by components (right) [2].

For the sake of diversity, particles deposit different amount of energy on different materials according to Bethe equation [4, 5]. Heavy charged particle e.g. protons and pions tend to lose energies by inelastic collision with electrons in the material. On the other hand, the incoming electron can undergo elastic collision and bremsstrahlung process which makes it loses energy faster than the heavy charged particles. This is also true for photon which loses its energy by pair production. The study of material budget is then based on the energy loss of electron and photon. The mean distance inside a material which high-energy electron loses all but 1/e of its energy or 7/9 of the mean free path for pair production by a high-energy photon is called the radiation length[6], X_0 [6]. The ratio between the actual length(x) that particle passes though the material and the radiation length (X_0) is used to compare the fraction of energy deposited on different materials.

The simulated material budget of CMS Tracker is shown in Fig.1.6 in the unit of radiation length [2]. The ratio of 1 means the electron loses all but 1/e of its energy (∼ 67%). It will lose all of its energy at the ratio of ∼1.58. From the graph, we can see that electron and photon lose a large portion of their energies in the Tracker and at some pseudorapidity (η) they even lose all of their energies before reaching Electromagnetic Calorimeter. Hence, in the next upgrade of the CMS Tracker, efforts are put into reducing the material budget in all possible parts including reducing cable materials, changing coolant, relocation of layers, and developing new readout electronics and sensor structure [7, 1].

One of the optional designs for the silicon strip sensor is to integrate the pitch adapter into the sensor. The pitch adapter is made of borosilicate glass with the total weight of 23.134 kg corresponding to 0.559% of the mass of the Tracker [3, 8]. Removing the PA will reduce the material budget of the Tracker by 0.003 - 0.045 x/X_0 [7]. More material budget can be reduced since the size of the supporting frame will also be reduced.

1.4.2 Flexibility of the Design of Sensor Modules

Eliminating pitch adapter creates rooms for new designs. The position of the frontend hybrid can now be adjusted and does not have to be at the end of the strip. The readout chip can be put directly on the sensor to utilize space efficiently. The cartoons of these designs are shown in Fig. 1.7.

---

[6] For the details and calculations of radiation length see Appendix A.3

[7] Self-calculation, See Appendix A.4

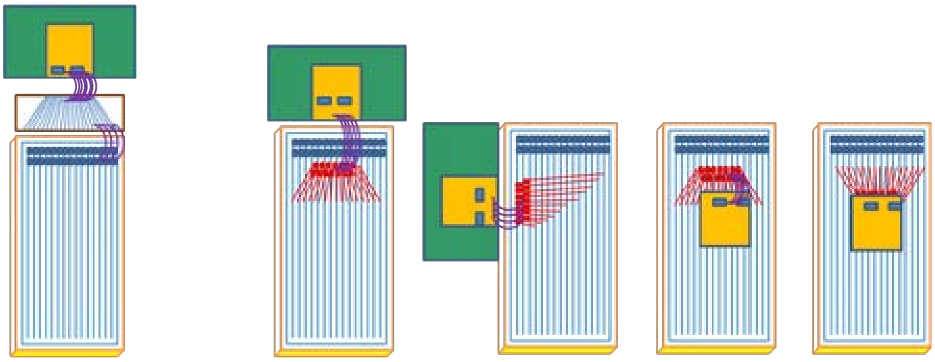

(a) (b)

Figure 1.7: a) current connection of pitch adapter to silicon strip sensor b) possible new designs: connect the front-end hybrid from the side of the sensor or put the readout chip directly above the sensor.

CHAPTER II

SILICON STRIP DETECTOR

The application of silicon detector is wide, ranging from CCD to photon, X-ray, Gamma ray, and charged particle detections. This chapter reviews the basic properties of silicon and the pn junction structure that is used in the charge detection device. Also, the designs of the current CMS silicon strip sensor and front-end electronics are discussed.

2.1 Basics of Silicon Properties

Silicon is an element in the 4th group of the periodic table. It is the second most abundant element in the earth crust. Some properties of silicon are summarized in Table 2.1. The advantages of silicon over other elements as a semiconductor material are 1) it is abundant, thus lower cost, 2) its natural oxide SiO_2 can be used as insulator, 3) changing of energy levels within the energy gap can be done by adding impurity atoms, and 4) the technologies are well established for producing high quality wafer. In this section, the band structure, the intrinsic and extrinsic properties of silicon will be disscussed.

2.1.1 Band structure

When consider one atom, the energy levels are discrete. When considering a crystal, the Pauli exclusion principle is still applied resulting in the very close discrete energy levels that become a band. The valence band is the outer most band that electrons are considered as bounded to the atom. The conduction band is the band that electrons have enough energy to move in the crystal lattice. The energy gap or the band gap is the difference between the highest energy point in valence band (valence band edge) and the lowest energy point in the conduction

Preperties of silicon	value
Atomic number	14
Atomic mass	28.0855
Density @ 300K (g/cm^3)	2.329
Crystal structure	Diamond
Lattice constant @ 300K	5.4 Å
Energy gap @ 300K (eV)	1.12
Energy to generate electron-hole pair @ 300K (eV)	3.62
Intrinsic carrier density @ 300K (cm^{-3})	1.5x10^{10}
Electron mobility @ 300K (cm^2[Vs]$^{-1}$)	1350
Hole mobility @ 300K (cm^2[Vs]$^{-1}$)	480

Table 2.1: Some properties of silicon [4, 9].

band (conduction band edge). The region in between is called the forbidden zone. In metal, there is no such gap and the valence electrons are thermally excited to the conduction band all the time. While in an insulator, the energy gap is so wide that the thermal energy is insufficient. In semiconductor, this gap is moderate and only some thermally excited valence electrons can jump to the conduction band. If the wave vector ($\vec{k}$) of the valence band edge and the conduction band edge are the same, the gap is called direct band gap. Otherwise, it is called indirect band gap.

Silicon is a natural semiconductor with the indirect band gap of 1.1 eV. This means that the valence electrons involve an indirect transition to the conduction band. Fig. 2.1 shows the energy band diagram of silicon. However, the generation of an electron-hole (e-h) pair requires a direct transition with the energy of 3.6 eV.

2.1.2 Intrinsic carrier concentration

Charge carriers in intrinsic semiconductor are electrons and holes. They are generated in pair and at the same time. When an electorn jumps to the conduction band, it leaves a hole in the valence band. Therefore, the electron density (n) and hole density (p) are the same. This is represented by the intrinsic carrier concentration (n_i) with $n_i = n = p$. Both carriers can move around when the electric

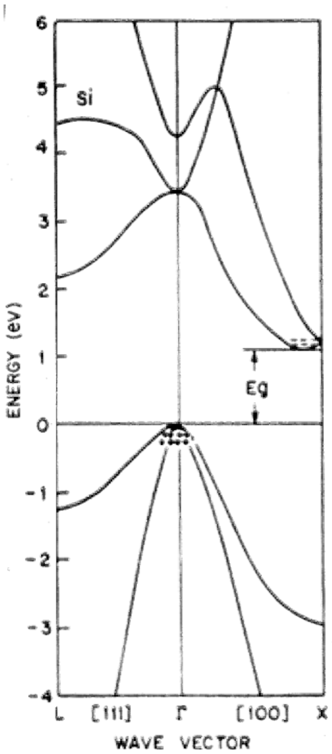

Figure 2.1: Energy band diagram of silicon[1].

field is applied. Intrinsic carrier concentration depends highly on temperature (T) and can be calculated from:

$$n_i = \sqrt{N_c N_\nu} exp \left(\frac{-E_g}{2kT} \right) \tag{2.1}$$

where $N_c = 2 \left(\frac{2\pi m_e^* kT}{h^2} \right)^{\frac{3}{2}}$ is the number of states in the conduction band,
$N_\nu = 2 \left(\frac{2\pi m_h^* kT}{h^2} \right)^{\frac{3}{2}}$ is the number of states in the valence band,
E_g is the energy gap,
m_e^* is the effective mass of electron,
m_h^* is the effective mass of hole .

2.1.3 Doping and PN Junction

Impurities can be added (doped) to the silicon crystal to increase the carrier density. There are two types of impurity: donor and acceptor. Group V elements, e.g. P, As, Sb; are donors. They have one valence electron more than that of silicon. The donor will add an energy level in the forbiden region close to

---

[1] Figure from: http://large.stanford.edu/courses/2007/ap273/hellstrom1/

the conduction band and donor electrons in this level will be easily thermally excited to jump to the conduction band. Therefore, the number of electrons in the conduction band is increased; while the number of holes in the valence band is the same. This type of silicon with electrons as majority carriers is called the n-type silicon. On the other hand, if silicon is doped with group III elements or acceptors; e.g. B, Al, and Ga, which have one less valence electron, the hole concentration in the valence band will increase. This is known as the p-type silicon. The change in energy level in the forbidden zone by various dopants is shown in Fig. 2.2. Normal doping concentration is $\sim 10^{13}$ atoms/cm^3 [4]. The highly doping concentration is $\sim 10^{20}$ atoms/cm^3 and is denoted with the plus sign e.g. p+, n++.

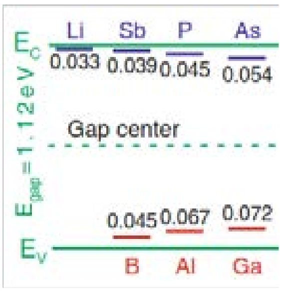

Figure 2.2: Energy levels of some impurities in the forbidden zone of silicon. Adapted from [9].

When p-type and n-type silicon are put into contact, the electrons from the n-side will combine with the holes in the p-side near the junction. The accumulation of electrons on the p-side and left-behind holes on the n-side will create a potential difference (built-in voltage, V_{bi}) across the junction which prevents further diffusion and recombination of the carriers. This will generate a region with no mobile carriers known as *depletion region* or *space charge region*.

The width of the depletion zone (W) can be changed by applying a voltage across the junction (Fig. 2.3). If the pn junction is forward-biased, the depletion zone will shrink and the current will start to flow through the junction. If it is reverse-biased, the space charge region grows and still no current flows. This property of reverse-biased pn junction can be used to detect charged particles as the e-h pairs in the depletion zone will only be created when charged particles pass through the region. More discussions on the reverse-biased pn junction are in the next section.

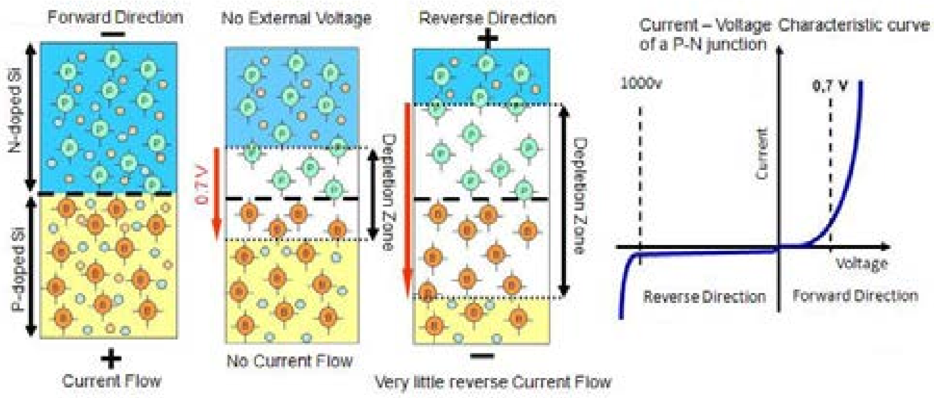

Figure 2.3: PN Junctions when (right) forward-biased (middle) no voltage is applied and (left) reverse-biased, and the current-voltage relation[2].

2.2 Reverse Biased PN Junction

2.2.1 Depletion voltage and Depletion width

Under reverse biasing, the charge carriers are attracted to the positive (Fig. 2.3), thus the depletion region grows. The applied voltage needed to fully deplete the sensor is called depletion voltage (V_{dep}). The expression for V_{dep} can be solved from Poisson's equation. It depends on the thickness (d) and the effective carrier concentration (N_{eff}) of the material.

$$\begin{aligned} V_{dep} + V_{bi} &= \frac{q}{2\epsilon\epsilon_0} \left| N_{eff} \right| d^2 \\ V_{dep} &\approx \frac{q}{2\epsilon\epsilon_0} \left| N_{eff} \right| d^2 \end{aligned} \tag{2.2}$$

where	V_{dep}	is the full depletion voltage,
	V_{bi}	is the built-in voltage created when the p-type and n-type materials are put into contact. This is usually neglected since $V_{bi} << V_{dep}$,
	N_{eff}	$= n - p + N_D - N_A$ is the effective carrier concentration with n and p are the intrinsic carrier concentration of the material, N_D and N_A are doner and acceptor concentration,
	ϵ	is the relative permittivity of the material,
	d	is the thickness of the material.

---

[2] Figure from: http://www.powerguru.org/p-n-junction/

Moreover, the expression for the depletion width (W) can be written as a function of reverse-biased voltage (V):

$$W(V) = \sqrt{\frac{2\epsilon\epsilon_0}{q_0 \left|N_{eff}\right|} V} \tag{2.3}$$

2.2.2 Capacitance-Voltage relation

The charge (Q) in the depletion region is proportional to the carrier concentration times the volume of the depletion region: $Q = eN_{eff}AW$, where A is the area and W is the depletion width. Since A is fixed and W is a function of V, the change of charge in the depletion region (dQ) is given by $dQ = eN_{eff}AdW$. When the region is not fully depleted, the capacitance is changed with the changing charge:

$$\begin{aligned} C = \frac{dQ}{dV} &= \frac{dQ}{dW}\frac{dW}{dV} \\ &= A\sqrt{\frac{\epsilon\epsilon_0 \left|N_{eff}\right|}{2V}} \quad \text{for } V < V_{dep} \end{aligned}$$

When the region is fully depleted, the capacitance becomes constant $C = Q/V = \epsilon\epsilon_0 A/d$. The expression for capacitance then becomes:

$$C = \begin{cases} A\sqrt{\frac{\epsilon\epsilon_0 \left|N_{eff}\right|}{2V}} & \text{for } V < V_{dep} \\ \frac{\epsilon\epsilon_0 A}{d} & \text{for } V > V_{dep} \end{cases} \tag{2.4}$$

This relations is used to determine the depletion voltage from the capacitance-voltage (CV) measurement. With the linear relationship between V and $1/C^2$, two straight lines can be used to fit the graph and the voltage at the intersection is determined as the depletion voltage (Fig. 2.4).

2.2.3 Leakage current

A small current generated when reverse biasing the pn junction is called the leakage current, reverse current or dark current. The first source of this current is from the diffusion of minority carrier to the electrode. This current is small and is in the order of nA/cm^2 [4]. The second source is from the impurities in the bulk material that create the intermediate states in the forbidden gap and act

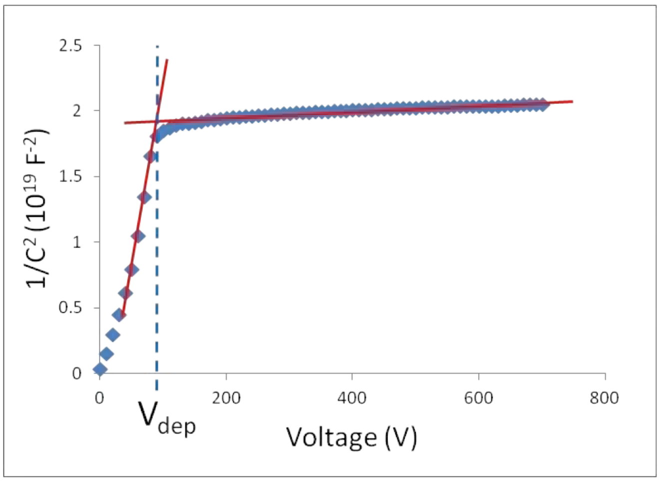

Figure 2.4: Determination of depletion voltage from capacitance-voltage relation.

as generation-recombination centers. The e-h pairs are thermally generated, thus this current depends highly on temperature and is in the order of μA/cm^2. The current - temperature relation is given by Eq.(2.5). This is used to scale the temperature down to the reference temperature (T_R). In this work, some of the current measurements were made at room temperature and were scaled down to $T_R = 20°C$ using this equation [11]. The third source of leakage current is from the surface current which involves the chemical reactions between interface of Si-SiO$_2$. In the case of unirradiated sensor, no charge presents in the insulator. Thus, this source is ignored.

$$\begin{aligned} I(T_R) &= I(T) \times R(T) \\ \text{with} \quad R(T) &= \left(\frac{T_R}{T}\right)^2 exp\left(-\frac{E_g}{2k_B}\left[\frac{1}{T_R} - \frac{1}{T}\right]\right) \end{aligned} \tag{2.5}$$

If the reverse-biased voltage reaches the breakdown voltage, the current will increase rapidly. This is due to either the avalance breakdown or the zener breakdown. The avalanche breakdown happens when the electric field is so large that the electrons in the e-h pairs have enough energies to further excite other electrons which further excites other electrons causing a very large number of e-h pairs. Zener breakdown occurs in a highly-doped pn junction which has a very thin depletion zone. Higher applied voltage increases the probability of the electrons from the valence band of the p side tunnel to the conduction band of the n side.

2.3 Signal Generation

Electron-hole pairs can be created in materials by the traversing of charged particles, photon interactions, and thermal excitation. The photon interactions include photoelectric effect, compton scattering, and pair production. In this work, signal in the test sensors are generated by the traversing of high energy electrons from Sr90 beta source. Hence, this section will focus on the signal generation by charged particles.

2.3.1 Signal generation by charged particles

When a charged particle travels through material, the energy loss rate depends on the properties of the particle e.g. charge, mass, speed; and the properties of the material. For heavy charged particles, the direction of their paths are assumed to be unchanged. The energy loss is mainly the result of inelastic collision with electrons in material (assumed to be free electrons) and elastic scattering from nuclei [4]. Then, the mean energy loss for the moderately relativistic heavy charged particles are described by Bethe equation (Eq. (2.6)).

$$\left\langle -\frac{dE}{dx} \right\rangle = Kz^2 \frac{Z}{A} \frac{1}{\beta^2} \left[\frac{1}{2} \ln \frac{2m_e c^2 \beta^2 \gamma^2 W_{max}}{I^2} - \beta^2 - \frac{\delta(\beta\gamma)}{2} \right] \tag{2.6}$$

where	$m_e c^2 = 0.511\,\mathrm{MeV}$	electron mass $\times c^2$
	$r_e = 2.818\,\mathrm{fm}$	classical electron radius
	$N_A = 6.022 \times 10^{23}\,\mathrm{mol}^{-1}$	Avogadro's number
	$K = 4\pi N_A r_e^2 m_e c^2$	
	z	charge of incident particle
	Z	atomic number of absorber
	A	atomic mass of absorber
	I	mean excitation energy in eV
	$W_{max} = \frac{2m_e c^2 \beta^2 \gamma^2}{1+2\gamma m_e/M+(m_e/M)^2}$	maximum energy transfer in a collision
	M	incident particle mass
	$\beta = v/c$	speed of incident particle in the unit of c
	$\gamma = \sqrt{\frac{1}{1-\beta}}$	
	$\delta(\beta\gamma)$	density effect correction to ionization energy loss

Fig. 2.5 shows the stopping power or the energy loss rate per density of material (in this case is copper) of a traversing particle (in this case muon) with different momenta. Bethe equation is applicable in the middle range including the minimum ionizing particle (MIP). At low momentum, the particle's speed is comparable to the speed of electrons in an atom and the binding energy of atomic electrons must be considered in energy loss calculation. While at the speed very close to the speed of light, particles tend to lose energy through radiative process [6] i.e. emiting new particles .

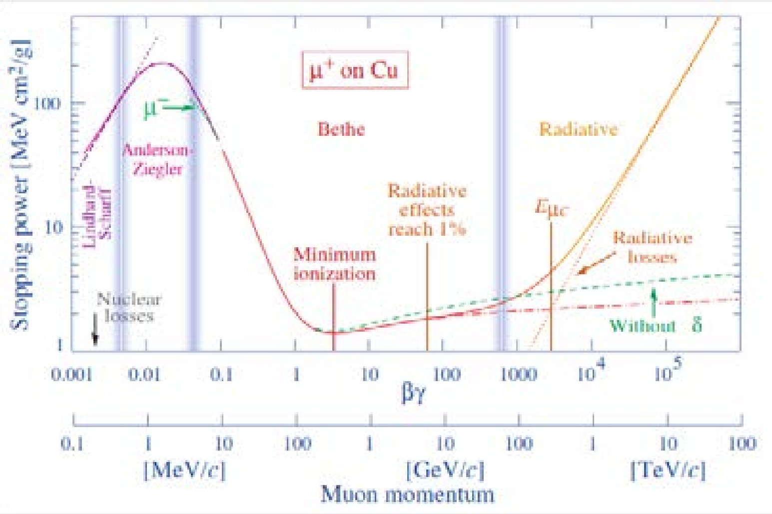

Figure 2.5: Energy loss rate of muon on Cu or the stopping power of Cu [6].

In case of electrons, because of their small masses the direction of their paths can be changed resulting in the domination of energy loss by bremsstrahlung for high energy electrons. Moreover, the indistinguishability of electrons has to be taken into account when considering the electron-electron collisions. The Bethe equation then becomes [6]:

$$\left\langle -\frac{dE}{dx} \right\rangle = \frac{1}{2} K \frac{Z}{A} \frac{1}{\beta^2} \left[\ln \frac{m_e c^2 \beta^2 \gamma^2 m_e c^2 (\gamma - 1)/2}{I^2} + (1 - \beta^2) - \; + \frac{1}{8} \left(\frac{\gamma - 1}{\gamma} \right)^2 - \delta \right] \tag{2.7}$$

The energy loss from the traversing particle is used to create e-h pairs in the material. In the present of an electric field, the generated e-h pairs will be separted and the signal is collected. Then, the distribuiton of the signal represents the distribution of the energy loss of the particle. In the thick material, this distribution approaches Gaussian distribution given by Eq.(2.8) with the mean energy loss equal to the mean of the distribution. However, in thin absorber, most particles loss small amount of energy and only little of particles loss large amount of energy in a single collision [4]. This is demonstrated in the long tail of the energy loss distribution. Landau distribution (Eq.(2.9)) is used to describe this phenomenon. In the real experiment, the convolution of both distributions is used to fit the data.

$$f_{Gauss}(d,x) \propto \exp\left(\frac{-(x-\bar{x})^2}{2\sigma^2}\right) \tag{2.8}$$

where d is the thickness of the material, x is the energy loss in the absorber, $\bar{x}$ is the mean energy loss, and σ is the standard deviation.

$$f_{Landau}(d,x) \propto \int_0^\infty \sin(2t)\exp\left(\frac{-t(x-\mu)}{\sigma} - \frac{2}{\pi}t\ln(t)\right)dt \tag{2.9}$$

where d is the thickness of the material, x is the energy loss in the absorber, μ is the most probable value of the energy loss (peak value in the distribution), and σ is the standard deviation.

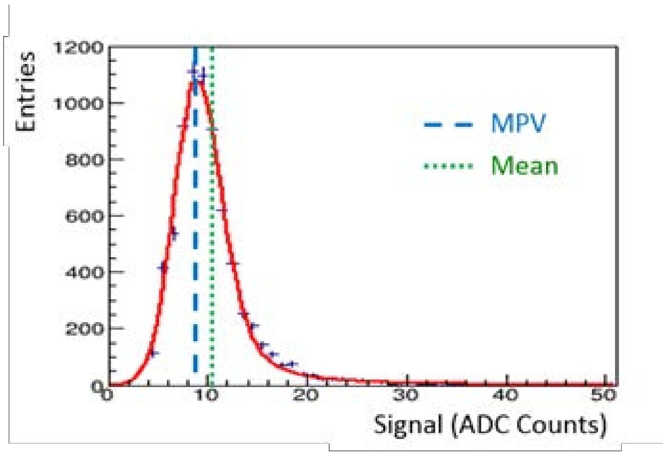

Figure 2.6: The distribution of energy loss in quite thin absorber.

In our analysis, these functions are calculated numerically in the analysis framework called ROOT[12]. The convolution of both function is done simply by multiplication.

Because the most probable value (MPV) of the energy loss distribution can be found directly from the fit and is more reliable than the mean value, it is common to used the MPV to represent the signal. Fig. 2.6 shows the position of the MPV and the mean value in the signal distribution. The ratio of the MPV to the mean value is ~0.8. For silicon, the mean energy loss rate calculated from the

Bethe's equation is ~390 eV/μm. Then, the MPV of the energy loss rate is ~312 eV/μm.

The number of e-h pairs generated in the material of thickness d can be calculated from Eq.(2.10) when the energy required to generate one electron-hole pair $\bar{E}_{gen}$ is known.

$$n_{e-h} = \frac{d \langle dE/dx \rangle}{\bar{E}_{gen}} \tag{2.10}$$

In the depletion zone, the effective doping concentration of the silicon is $\sim 10^{12}$ atom/cm^3, while there are $\sim 10^{22}$ silicon atom/cm^3. Therefore, the energy required to generate an e-h pair is essentially that of the silicon which is 3.6 eV. With the mean energy loss, about 22,000 e-h pairs are generated in 200-μm-thick silicon wafer. This gives the MPV of ~17,300 e-h pairs.

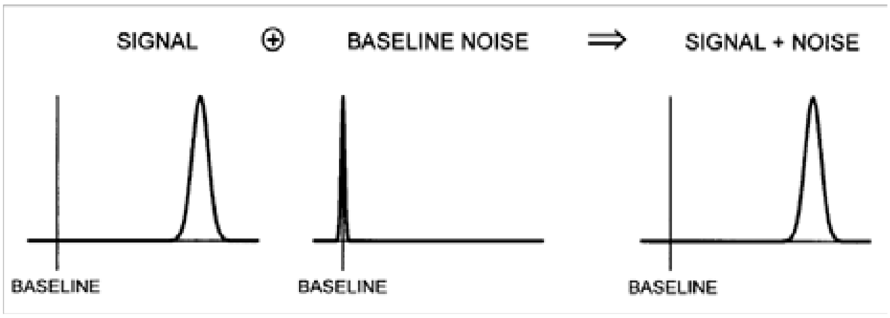

Figure 2.7: The contributions to the measured signal are from the distribution of signal and base line noise [13].

2.3.2 Noise

Noise is the fluctuation of baseline. Fig. 2.7 shows the distribution of signal, baseline noise, and signal plus baseline noise. The noise broaden the signal distribution thus reducing the resolution of the detector, which is defined as (FWHM of signal distribution)/(value of signal at peak). In the detector that we are interested in, a pulse current from the sensor will be amplified with charged sensitive preamplifier in the readout chip (more in section 2.5). The sources of noise are from 1) preamplifier 2) shot noise from leakage current and 3) thermal noise from parts with resistance. Noise of the preamplifier is a function of total input capacitance. Then, this noise can be minimized by putting the preamp as close to the sensor as possible [4]. Shot noise occur from the fluctuation of number of carriers that constitutes the current pulse. Thermal noise occur from the fluctuation of velocity of carriers due to the heat from resistor. Thermal noise and shot noise are totally random[13]. A summary of noise estimation in CMS silicon strip detector module can be found in [14, 15]. The signal to noise ratio (S/N) of greater than 9 ensures the track finding efficiency of greater than 95% [17].

2.4 CMS Silicon Strip Sensor

As its name suggests, the silicon strip sensor consists of many parallel implanted strips on the bulk silicon wafer. The implants and the bulk material constitute the pn junctions. Each strip is independent and act as a charge collecting electrode. When a charged particle passes through the sensor, a strip or a few strips are triggered, thus a 1D position of that particle is known. By using multiple layers and by arranging the direction of the strips, one can get a 2D position e.g. like the net of a tennis racket. In CMS detector, there are 10 cylindrical layers with some of the layers being double-sided detector modules.

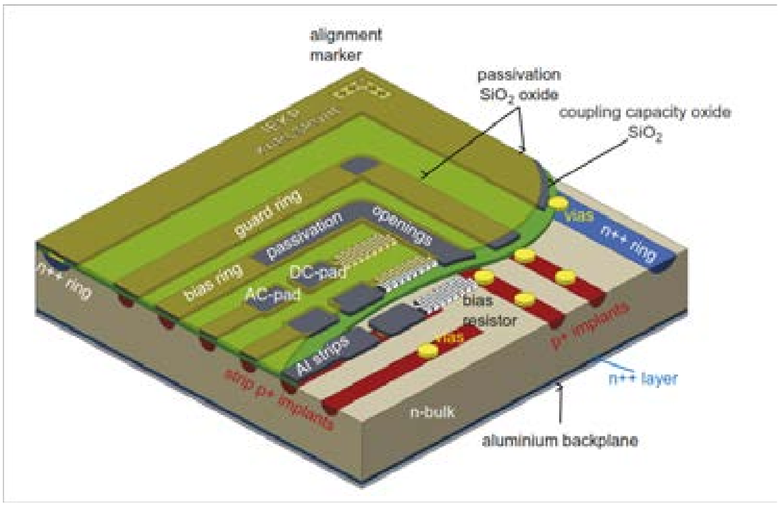

Figure 2.8: Structure of an n-type CMS silicon strip sensor [10].

The structure of the current CMS silicon strip sensor is shown in Fig. 2.8. The p-type strips are implanted into an n-type wafer. The strips are surrounded by two rings. The inner ring is the *bias ring* which is connected to the *bias resistors* of each strip. The outer ring is the *guard ring* which is used to stabilize the electric field for the edge strips. The *bias resistor* is connected, on the other side, to the implant strips. The metal (aluminum) strip lies precisely on top of the implanted strip separated by an insulator layer. The signal on the aluminum strips are generated by a capacitive coupling to the implanted strips i.e. the accumulation of charges on an implanted strip induces a collection of charges on the metal strip through the dielectric insulator. The connections to the readout electronics is then made at the *AC-pad* on the metal strip. Another readout connection is at the *DC-pad* which is connected directly to the implanted strip via the ohmic contact known as *via.* The DC-pads are used for testing and characterizing the sensor.

As discussed in section 1.3, the sizes of the sensors are different depending on the position inside the Tracker. Fig. 2.9 shows different geometries of the silicon strip sensors used in the CMS detector.

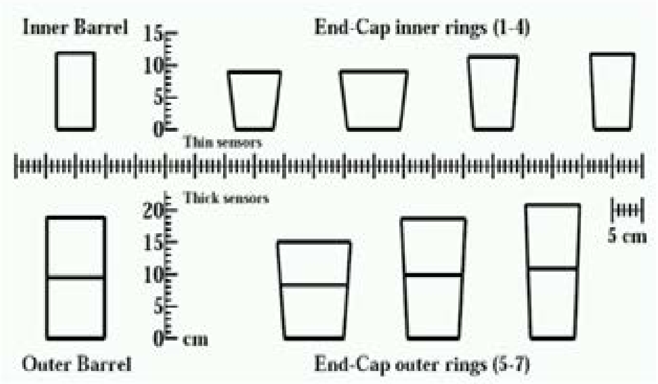

Figure 2.9: The geometries of silicon strip sensors labeled by position in the CMS Tracker [2].

2.5 CMS Front-end Readout Electronics

Fig. 2.10 presents the components of CMS silicon strip detector module which are the sensors, the pitch adapter, the front-end electronics, and the supporting structure. The front-end hybrid, the first part that process the signal from the strip sensor, is composed of 4 APV25 readout chips, an APVMUX, a TPLL, and a DCU (See Fig. 2.11).

APV25 is a readout chip that use Analogue Pipeline-Voltage mode. Fig. 2.12 shows the schematic diagram of the components of the APV25 chip. One chip has 128 channels connected to 128 strips of the silicon strip sensor. Each of the metal strips of the sensor is connected to a charge-sensitive preamplifier in the APV25. A pulse current from the metal strip induces charge in the capacitor of the charge-sensitive preamplifier. The analogue voltage proportional to the amount of induced charges is output from the preamplifier and is fed into a switchable inverter. A CR-RC shaper shapes the voltage pulse with the rise time of 50 ns. The signal is then sampled at 40 MHz (every 25 ns) or 20 MHz (every 50 ns) into a pipeline which stores 192 consecutive readout voltage. The element that has high value (peak mode or deconvolution mode) is selected by the processor called Analogue Pulse Shape Processor (APSP). The output from all 128 channels is combined by the multiplexer into 1 output with header, address, error value, analogue signal from 128 channels, and sync pulse.

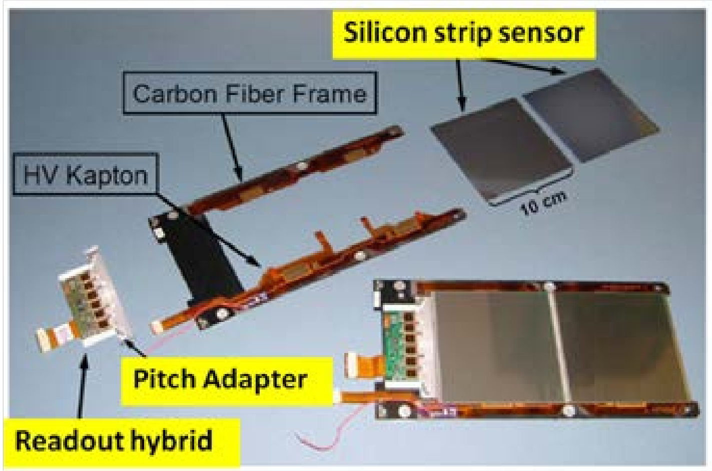

Figure 2.10: CMS TOB module. Adapted from [10].

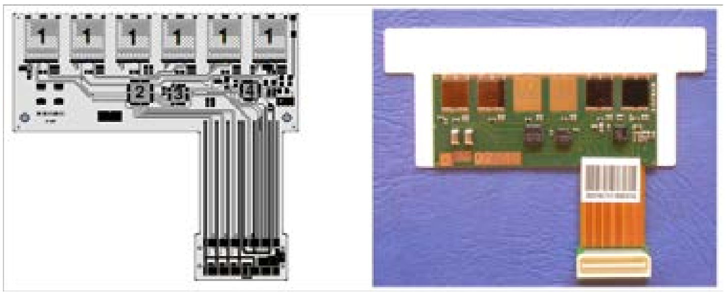

Figure 2.11: Front-end readout hybrid of Tracker End Cap (TEC) module with 1-APV25 chips, 2-APVMUX, 3-TPLL, and 4-DCU [14].

APVMUX: APV Multiplexer is used to combine signal from 4 APVs into a single output line.

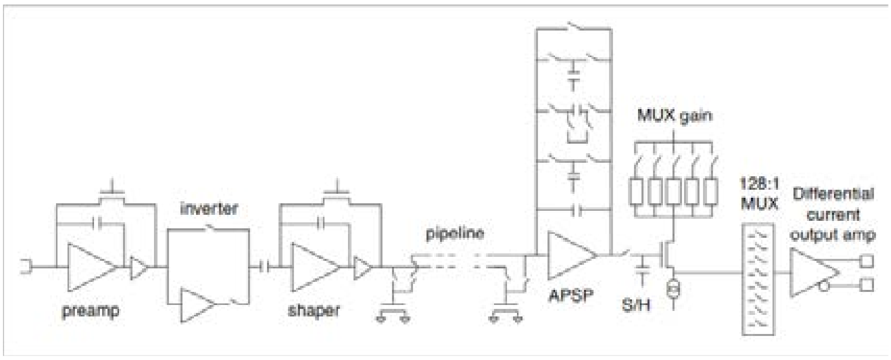

Figure 2.12: Block diagram of APV25 readout chip. The electronics chain before 128:1 MUX is for one channel [16].

TPLL: Tracker Phase-Locked Loop is used to sync clock and trigger signal from the external controller.

DCU: Detector Control Unit is used for monitoring voltage and temperature levels of the front-end electronics.

More details can be found on [14, 15, 16].

CHAPTER III

SILICON STRIP SENSOR WITH INTEGRATED PITCH ADAPTER

The study of silicon strip sensor with integrated pitch adapter is one of the optional design for new upgraded CMS Tracker sensors. The qualified manufacturer is the Hamamatsu Photonics K.K. (HPK) company. The campaigns to study new sensor with radiation hard properties and new designs are based on the sensor from this company. This chapter describes the test structures used in our study and reviews the previous works on the sensors with integrated pitch adapter. The main literatures on the previous works are from Hoffman et al. [18], Dragicevic [19], and Eber [20].

3.1 CMS Tracker collaboration and HPK campaign

The CMS Tracker collaboration consists of more than 70 institutions from 13 countries. The main duty is the supervision of the pixel and strip detectors both hardware and software parts. There are many tasks going on in parallel e.g. sensors and readout electronics development, tracking software development, upgrade simulations, calibration and performance measurement.

The HPK campaign is the study of the future silicon sensors fabricated by the HPK company, in the search for radiation hard sensors, better designs, and material reduction. The test structures are designed to fit in the 6” silicon wafer mask (Fig. 3.1). Different materials, fabrication methods, thickness, and designs are varied [22, 23]:

Float zone (FZ) The standard method used to grow silicon crystal is by bringing the polysilicon rod into contact with seed crystal and locally melt the rod. The impurity will stay in the melting zone, thus purifying the crystal. In the HPK campaign, the thickness of the float-zone silicon are 320, 200 and 120 μm.

Magnetic Czochralski (MCz) The silicon is melted. The seed crytal is put into contact with the melt and pulled up. This method helps creating crystal with high oxygen content which has previously shown radiation hard properties. The thickness of 200 μm is studied in the HPK campaign.

Epitaxial (Epi) Chemical Vapor Deposition method is used to grow a very thin silicon crystal. This comes with the thickness of 100 and 50 μm in the HPK campaign.

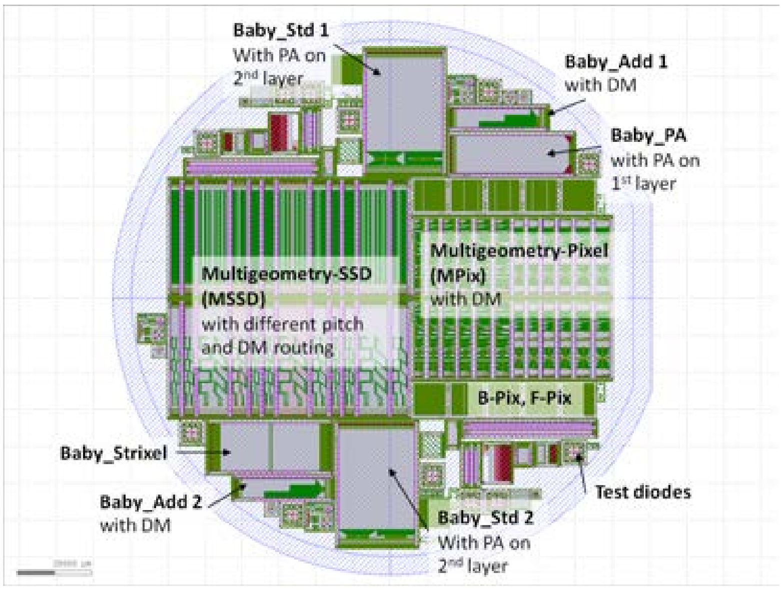

Figure 3.1: Test sturctures in the same 6” wafer.

Different materials are n-type (N) and p-type sensors. The type of the sensor is named after type of the bulk material. P-type sensors come with two different charge separation structures: p-stop (P) and p-spray (Y). Fig. 3.2 shows the three types of sensor materials.

p-stop p-type implants between n-type strips as a charge separation

p-spray thin layer of p-type sprayed in the region between n-type strips

Different sensors in the wafer are used for different studies e.g. the MSSD sensors have 12 regions of different pitches and implant widths, the MPix sensors have 12 regions of different pixel lengths and width/pitch, and small diodes for annealing study. Different wafers have different structures and materials. In our study, the sensors in the wafer come with the double metal (DM) routing (Fig. 3.1). The green lines represent the routing on the second layer. In this work, the baby additional (Baby add) sensors with double metal layer are studied to see the effect of the double metal and the length of the routing. The details of the sensor structure are discussed in the next section.

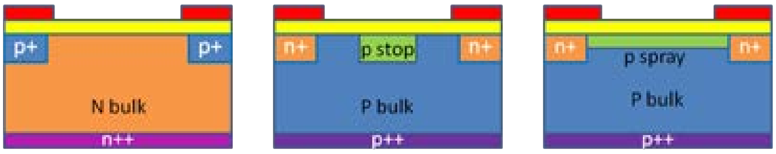

Figure 3.2: Sensor materials: N-type, P-type with p-stop, and P-type with p-spray.

3.2 Double Metal Sensor Design

In 2.4, the design of the current CMS Tracker sensor was discussed that the metal strips are floating over the implants separated by an insulator. This metal layer will be referred to as the first metal layer. The second metal layer is above the first metal layer separated by insulator. At the end of the metal strip on the second layer, an ohmic contact to the metal strip on the first layer is made via the *via*. Fig. 3.3 displays the schematic structure of the double metal sensor.

The baby additional (Badd) strip sensors tested in this work are 200 μm thick with the two metal layers separated by a 1.3 μm thick insulator [24]. Fig. 3.4 shows three different routing lengths of the double metal layer: 0, 7 and 14 mm measuring from the wide end of the pitch adapter. The design of the pitch adapter on the Badd sensors is based on the shortest metal routing [19]. The strip pitch is 80 μm wide. There are two designs of the Pitch Adapter (PA): the first design (Badd_1) adapts from 80 to 44 μm pitch and is connected to every strip, the second design (Badd_2) adapts from 160 to 44 μm pitch and is connected to every other strip.

The naming convention for the test sensors is FabricationThicknessType_WaferNumber_Structure_StructureNumber. There are 6 sensors tested in this work. All of them are Float zone:

F200DN_01_Badd_1
F200DP_05_Badd_1
F200DY_07_Badd_1
F200DN_04_Badd_1
F200DP_04_Badd_2
F200DY_05_Badd_2

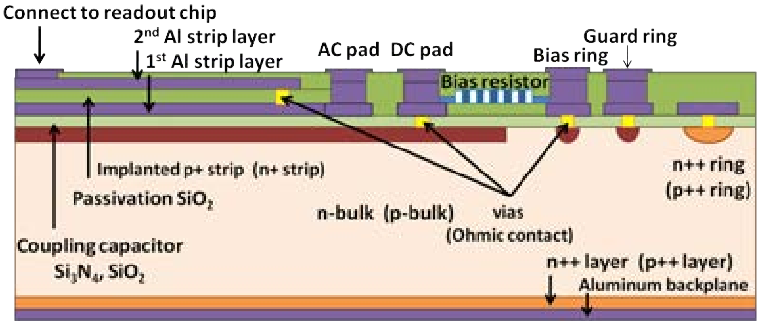

Figure 3.3: Longitudinal cross section of the double metal sensor.

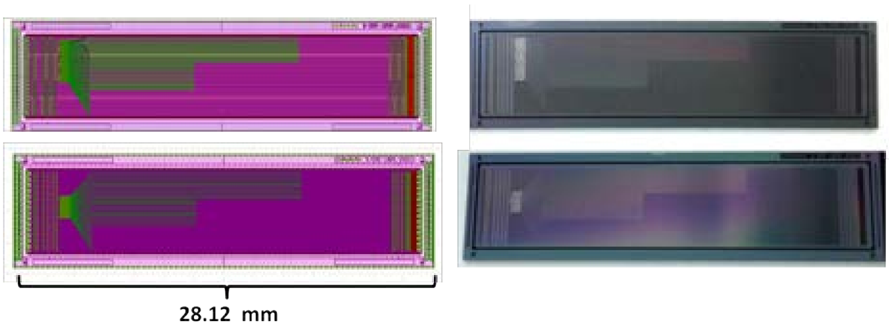

Figure 3.4: Two designs of PA on baby additional strip sensors. The green lines show the routing on the second metal layer. Top: the first design (Badd_1), Bottom: the second design (Badd_2).

3.3 Expected Behavior Before Irradiation

The previous works on unirradiated sensors with integrated PA came from Hoffmann et al. in 2010 [18, 19] and Eber in 2011 [20, 24]. Hoffmann et al. studied sensor with integrated PA on the first and the second metal layer. The results

	Thickness (μm)	dE/dx (eV/μm)	E_{gen} (eV)	Charge generation
Silicon (sensor's bulk)	200	390	3.6 (per e-h pair)	~22,000 e-h pairs
Aluminum (metal strips)	4	440	4.26 (work function)	~400 electrons

Table 3.1: Comparation of signal generated in silicon bulk and in metal strip

showed lower signal to noise ratio (S/N) and chances of cross-talk in the PA region on the first metal layer. Unfortunately, the sensor with PA on the second metal layer had many bad channels due to the low quality insulation layer. Therefore, no conclusion was made on this. The more recent study from Eber on the HPK sensor with integrated PA on the first and the second metal layer revealed similar results for the PA on the first metal layer. For the PA on the second metal layer, no reduction in S/N is found. However, the study on irradiated sensor was not performed. In this section, the expected behavior before irradiation is discussed.

3.3.1 Signal

From section 2.3.1, the energy loss of MIP in material can be calculated from Bethe equation. To compare between silicon bulk and the metal strip, Table 3.1 summarizes the number of carriers generated. However, since there is no electric field in the metal strip, no signal is expected from the metal strip.

3.3.2 Coupling between implant and metal strip

Fig. 3.5a shows the integrated PA on the first metal layer. One end of the metal routing is turned into the pitch adapter. The results from [18] show the reduction in S/N when the source is put over the PA region (Fig. 3.5). This is because in the PA region, the implants are not fully covered by the metal strip. Thus, the accumulated charges on the implants have to travel some distances to induce the signal in the metal strip and due to the resistance of the implants, some charges are lost. The crossing of metal strips above many implants also induce the cross talk.

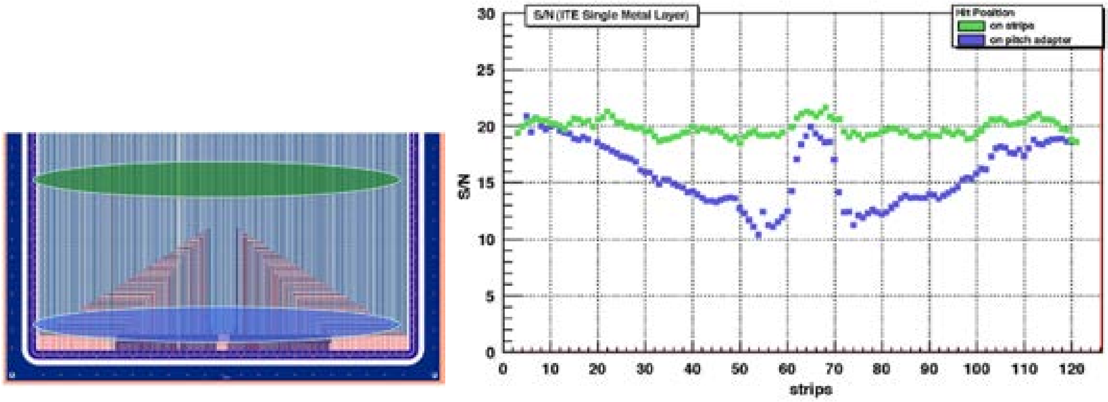

(a) (b)

Figure 3.5: a) Positions of beta source over the sensor b) Signal to noise ratio from the sensor with integrated PA on the 1st layer [18].

The study of sensor with integrated PA on the second metal layer was done by Eber. Fig. 3.6a shows the PA on second metal layer with the design based on shortest routing lines. Fig. 3.6b shows the S/N which are quite stable over all strips except for some bad channels in the middle. The conclusion from his study is that the concept of DM is proven to be working. However, the study on the irradiated sensor has not been done.

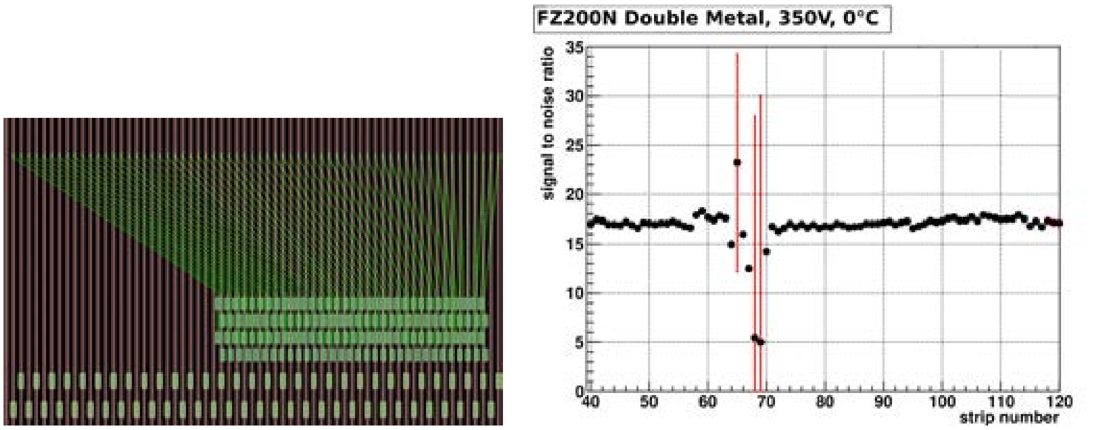

(a) (b)

Figure 3.6: Sensor with integrated PA on 2nd metal layer a) PA design b) Signal to noise ratio [20].

3.4 Expected Behavior After Irradiation

3.4.1 Proton irradiation

The CMS Tracker is suffering from many type of radiation: photons, charged hadrons, neutral hadrons, muons. Fig. 3.7 shows the fluence of charged hadron as a function of radius of CMS detector at 14-TeV pp collider with the integrated luminosity of 100 fb^{-1} expected after year 2020. In this study, some of the test sensors were irradiated with 800 MeV proton to the fluence of 0.8×10^{15} cm^{-2} at the Los Alamos National Laboratory. This fluence is comparable with the charged hadron fluence for the radius of 10 cm in the graph.

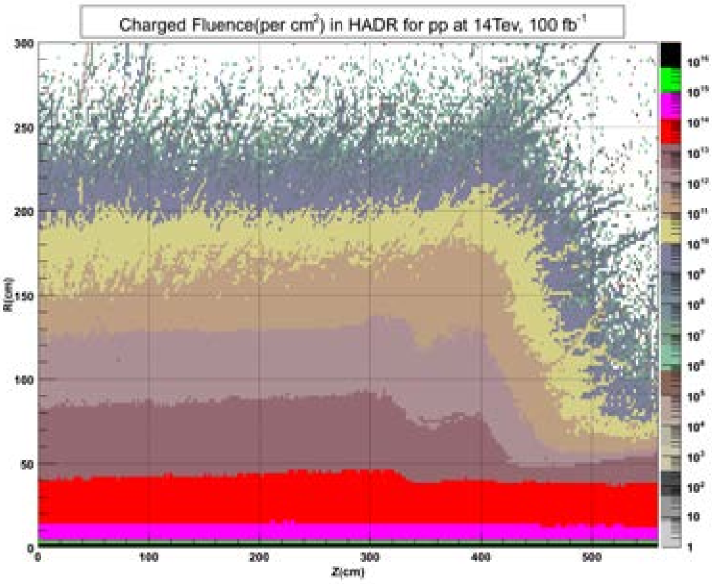

Figure 3.7: Charged hadron fluence in CMS detector simulated at 14 TeV, 100 fb^{-1}[25].

3.4.2 Effect of irradiation on electrical properties of the sensor

Main effect of irradiation on sensor is the generation of defects in the crystal structure. These defects are caused by high energy particle knocking atom out of its lattice site generating a vacancy in the lattice and an interstitial atom. Defects can propagate around, combine with impurity atom or form a more complex structures with other defects. These defects create intermediate states in the energy gap which results in many macroscopic effects. Fig. 3.8 shows the energy levels of defects and their corresponding effects. An increase in leakage current is the result of the defect level in the middle of the energy gap that requires less energy to generate e-h pair. The defect levels closed to E_C or E_V will increase the carrier concentration which will result in the rise of depletion voltage according to Eq. (2.2). The shallow defect levels will cause the charge trapping. The carrier is trapped for a short period of time and is released later. This affects the charge collection efficiency and charge sharing behavior of the sensor.

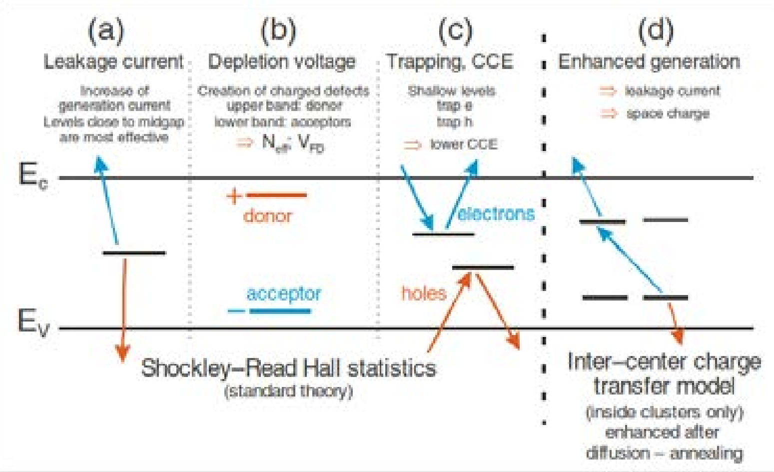

Figure 3.8: Defect levels and their corresponding macroscopic effects [10].

3.4.3 Effect on double metal

Different materials require different amounts of energy to knock atoms out, which is known as the threshold displacement energy (E_{dist}). This value is used to determine the radiation hardness of material. For the test sensor, the threshold displacement energies of silicon, aluminum, and the insulator (SiO_2 and Si_3N_4) are 15, 16, and 20-40 eV, respectively . The differences between the strips with, and without, DM are the layer of metal strips and the insulator layer, which has a similar thickness (∼4 µm). Different defects can be formed in two cases. However, due to the small thickness, little difference in signal is expected between them.

CHAPTER IV

ELECTRICAL PROPERTIES MEASUREMENT

The purpose of electrical properties measurement of the test sensors is to check the quality of the test sensors before signal measurements. The CMS specification for silicon strip sensor is given by [27].

4.1 Setup

Fig. 4.1 shows the probe needle station at Brown University. On the left of the setup are a high voltage power supply and nanoammeter (Keithley 6517B), an LCR meter (HP LCR 4284A), multimeters (Keithley's) connected to temperature sensors and humidity sensor, Power supply for Peltier elements, and a switch box to switch between current measurement and capacitance measurement. The sensor is placed on the aluminum chuck and secured by the vacuum suction. The chuck is cooled by 4 Peltier elements and a liquid cooling system. It can be cooled down to -20°C without any condensation problem by using an almost-air-tight lid and by flushing in extra dry air. Another purpose of the lid is to keep the sensor away from light during the measurement since light can generate signal thus increases the measured current. The sensor is biased between the back plane and the bias ring on the top of the sensor. This is done by applying the voltage between the cold chuck and a probe needle connected to the bias ring. The probe needle's tip is originally 7μm in diameter. The needle is operated by a micromanipulator. The connection of the needles to the sensor was made under a microscope. The measurement is controlled by an in-house LabView program.

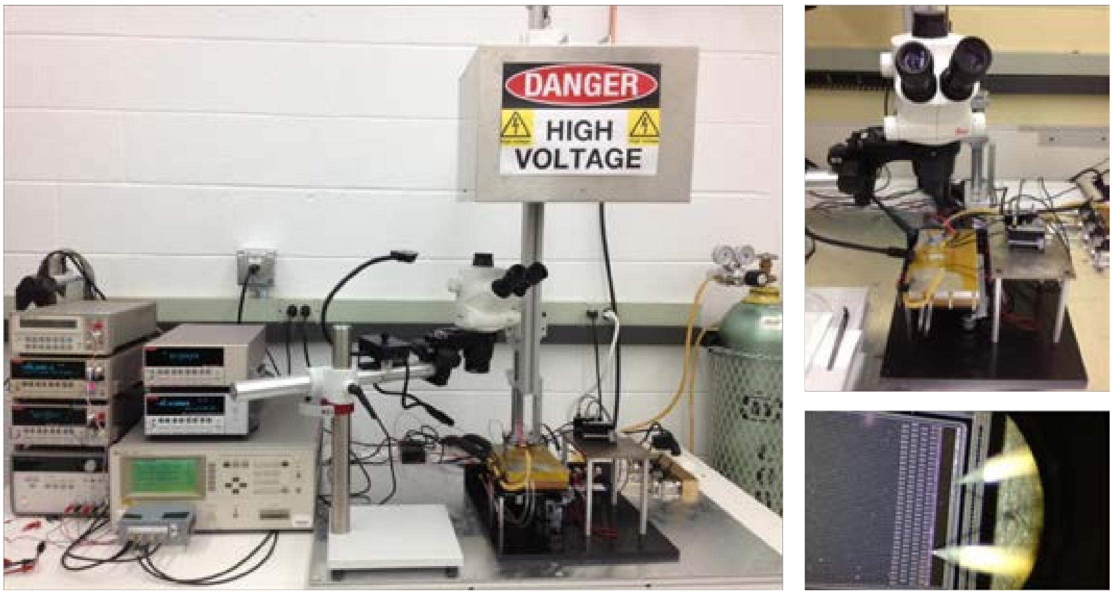

Figure 4.1: Electrical properties measurement setup at Brown University.

4.2 Measurement

The measurement method is followed directly from chapter 5 of [26]. The measurements were done at room temperature (RT). For single strip test, only 10 strips were tested: 1, 9, 18, 22, 30, 37, 44, 51, 57, 64. The electrical properties that were measured are:

- **Total leakage current (IV)**
- **Total capacitance (CV)**
- **Single strip leakage current (Ileak)**
- **Bias resistance (Rbias)**
- **Coupling capacitance (CC)**
- **Inter-strip capacitance (InterC)**
- **Short measurements**

4.2.1 Total leakage current (IV)

The circuit and connections for IV measurement are shown in Fig. 4.2. The voltage was applied between the back plane and the bias ring. The current read from the bias ring is the total leakage current of the sensor. The voltage was increased from 0 to 700V with 10V steps. The measurements were done at RT, 0°C and -20°C.

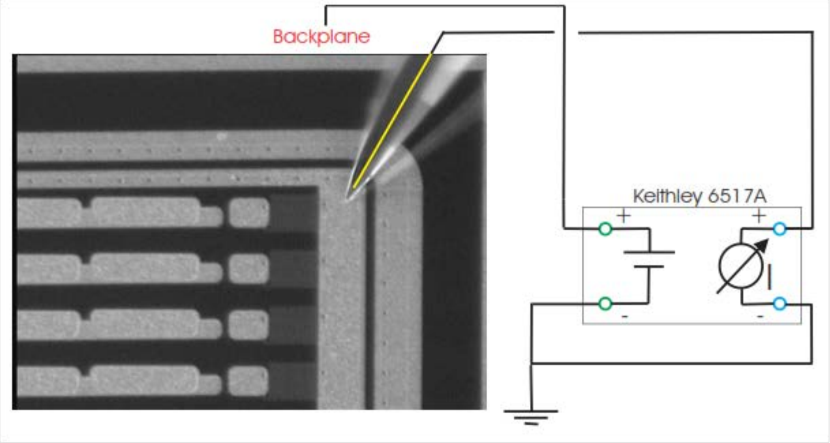

Figure 4.2: IV measurement scheme [26].

4.2.2 Total capacitance (CV)

The capacitance-volatge relation was measured using LCR meter (Fig. 4.3). The ISOBOX is used to add the applied voltage from Keithley 6517B to the voltage from LCR meter and to prevent the damage from leakage current to the LCR meter. The total capacitance of the bulk of the sensor was measured with the applied voltage ranging from 0 to 700V with 10V steps. The measurements were doned at 1,000 Hz and 10,000 Hz at RT, 0°C and -20°C.

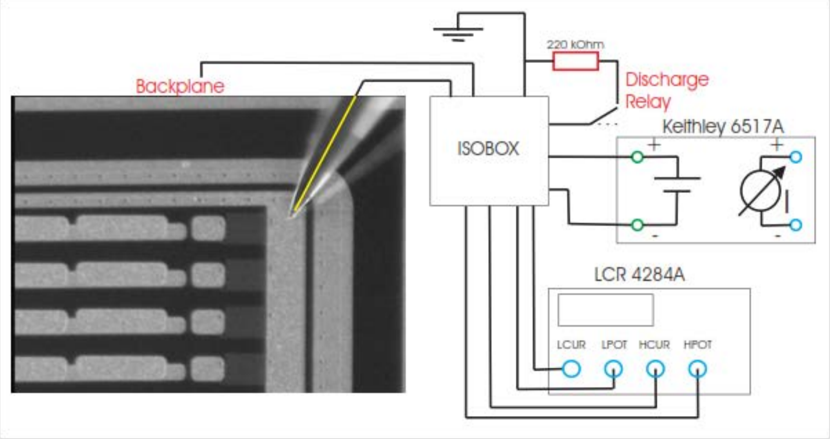

Figure 4.3: CV measurement scheme [26].

4.2.3 Single strip leakage current (Ileak)

One needle connected to the bias ring was used to applied the voltage to the sensor (Fig. 4.4). Another needle was used to read the leakage current from any particular strip. The measurements were done at RT.

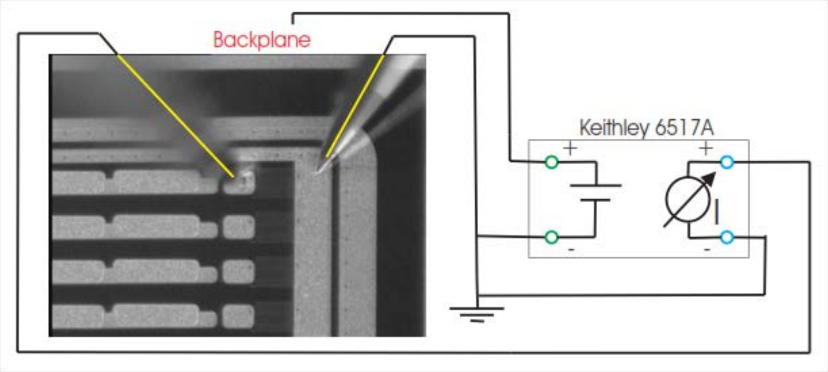

Figure 4.4: Single strip leakage current measurement sheme [26].

4.2.4 Bias resistance (Rbias)

The connection for measuring bias resistance is similar to the single strip leakage current measurement (Fig. 4.5). A small voltage of 2V (V_{meas}) was applied between the two needles forcing the current to flow through the bias resistor. The currents were measured from the needle connected to the bias ring (I_{meas}). When I_{leak} is known from the single strip leakage current measurement, the bias resistance can be calculated from Eq. (4.1). The measurements were done at RT on selected strips.

$$\begin{aligned} R_{bias} &= \frac{V_{meas} V_{bias}}{(I_{meas} - I_{leak})(V_{bias} - V_{meas})} \\ &\approx \frac{V_{meas}}{I_{meas} - I_{leak}} \end{aligned} \tag{4.1}$$

4.2.5 Coupling capacitance (CC)

The coupling capacitance between the implanted strips and the first layer metal strips were measured at 10,000 Hz, at RT. The connections are shown in Fig. 4.6.

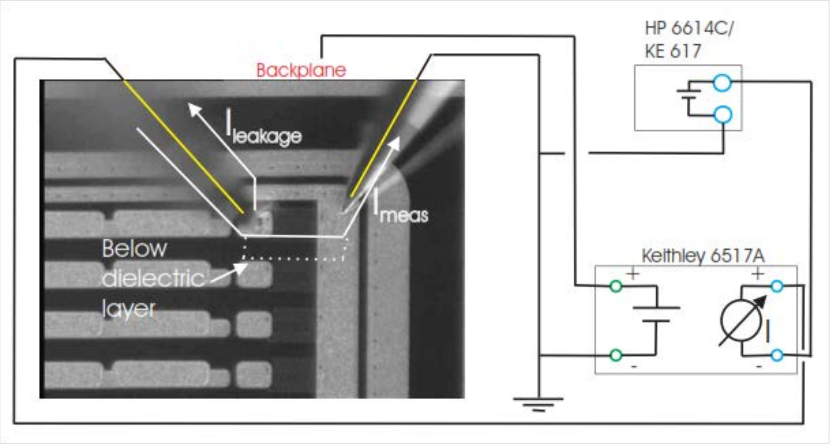

Figure 4.5: Bias resistance measurement scheme [26].

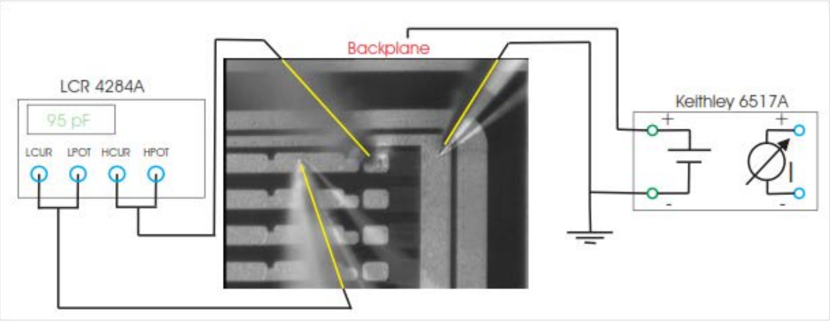

Figure 4.6: Coupling capacitance measurement scheme [26].

4.2.6 Inter-strip capacitance (InterC)

The capacitance between two strips were measured at 1MHz, at RT. The selected pairs are 1-2, 8-9, 22-23, 30-31, 37-38, 44-45, 50-51, and 63-64. The connections of the needles are shown in Fig. 4.7.

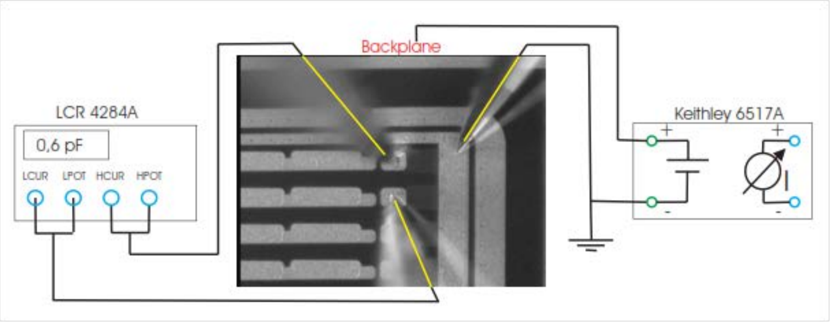

Figure 4.7: Inter-strip coupling capacitance measurement scheme [26].

4.2.7 Short measurements

Short between implanted strips and metal strips were tested by observing if there is current between the two strips or not. A strip is defined as short if the the current is more than 1 nA at 10V.

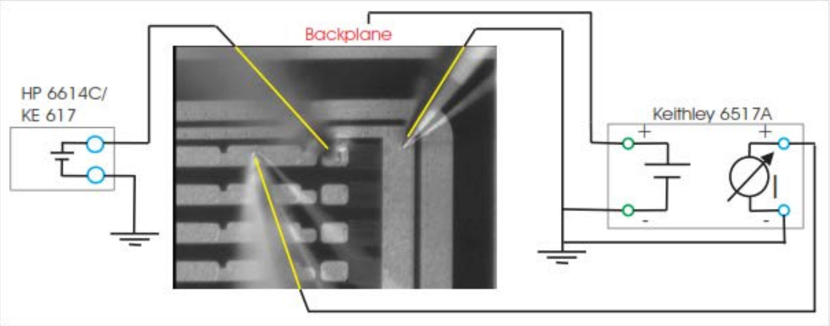

Figure 4.8: Short measurement scheme [26].

4.3 Analyses and Results

The measured data was written into text files. ROOT macros are implemented to plot and calculate parameters. The source codes in C++ were first developed by Zaixing Mao, a PhD student in the experimental particle physics laboratory at Brown University, for analyzing diode data. I have modified the code to use with strip sensor.

Depletion voltage and total leakage current

As discussed in section 2.2, the capacitance-voltage relation is given by Eq. (2.4). The two straight lines are used to fit the graph to find the depletion voltage. Fig. 4.9 shows CV and IV measurements for F200DP_04_Badd_2 sensor. The leakage current was scaled from room temperature down (orange dots) to 20°C (blue dots) using Eq. (2.5). At the bottom of the graph, the temperature (filled circles) and the dew point (open circles) at the times of the measurements are shown. On the right of the graph, the depletion voltage (V_{dep}), final capacitance (C_{final}), Thickness, effective doping concentration ($|N_{eff}|$) are shown. For HPK campaign, depletion voltages (V_{HPK}) are stored at 1.2 times of V_{dep}. Other parameters, i.e. final capacitance (C_{HPK}), total leakage current (I_{leak}); are read at V_{HPK}.

For the specification [27], the depletion voltage must be less than 300 V. The total leakage current must be less than 10 μA at 300 V. Fig.4.10 and 4.11 summarize the depletion voltages and total leakage currents of all test sensors.

Single strip leakage current

Single strip leakage current (I_{leak}) must be less than 100 nA at 400 V [27]. I_{leak} of F200DP_04_Badd_2 as shown in Fig. 4.12a follows this specification. Fig. 4.12b shows the single strip leakage currents read at the depletion voltages of all sensors.

Bias resistance

The bias resistances must be in the range of 1.5±0.5 MΩ and are uniform within one sensor (±0.3 MΩ) [27]. Bias resistances of 4 test sensors are shown in Fig. 4.13.

Coupling capacitance

The coupling capacitance must be greater than 1.2 pF/cm per µm of implanted strip width [27]. The strip length of the test sensor is 2.48 cm with the strip width of 20 μm. The coupling capacitance for the test sensors must then be greather than 59.5 pF. All test sensors satisfy this condition (Fig. 4.14).

Inter-strip capacitance

The total capacitance equals the sum of the coupling capacitance to two neighbring strips on each side and the capacitance to the back plane ($C_{tot} = C_{int} + C_{back}$). Then C_{tot} must be less than 1.3 pF/cm [27]. The inter-strip capacitance measurements were done with only one neighbor. Fig. 4.15 summarizes the values for all test sensors. As an example, the total capacitance of F200DP_04_Badd_2 can be calculated from $C_{int} \sim 0.4$ pF and, from Fig. 4.9, $C_{back} \sim 72$ pF/64 strips ~ 1.125 pF. C_{tot} is then approximately $(4(0.4) + 1.125)/2.48 \sim 1.1$ pF/cm which is in accordance with the CMS specification.

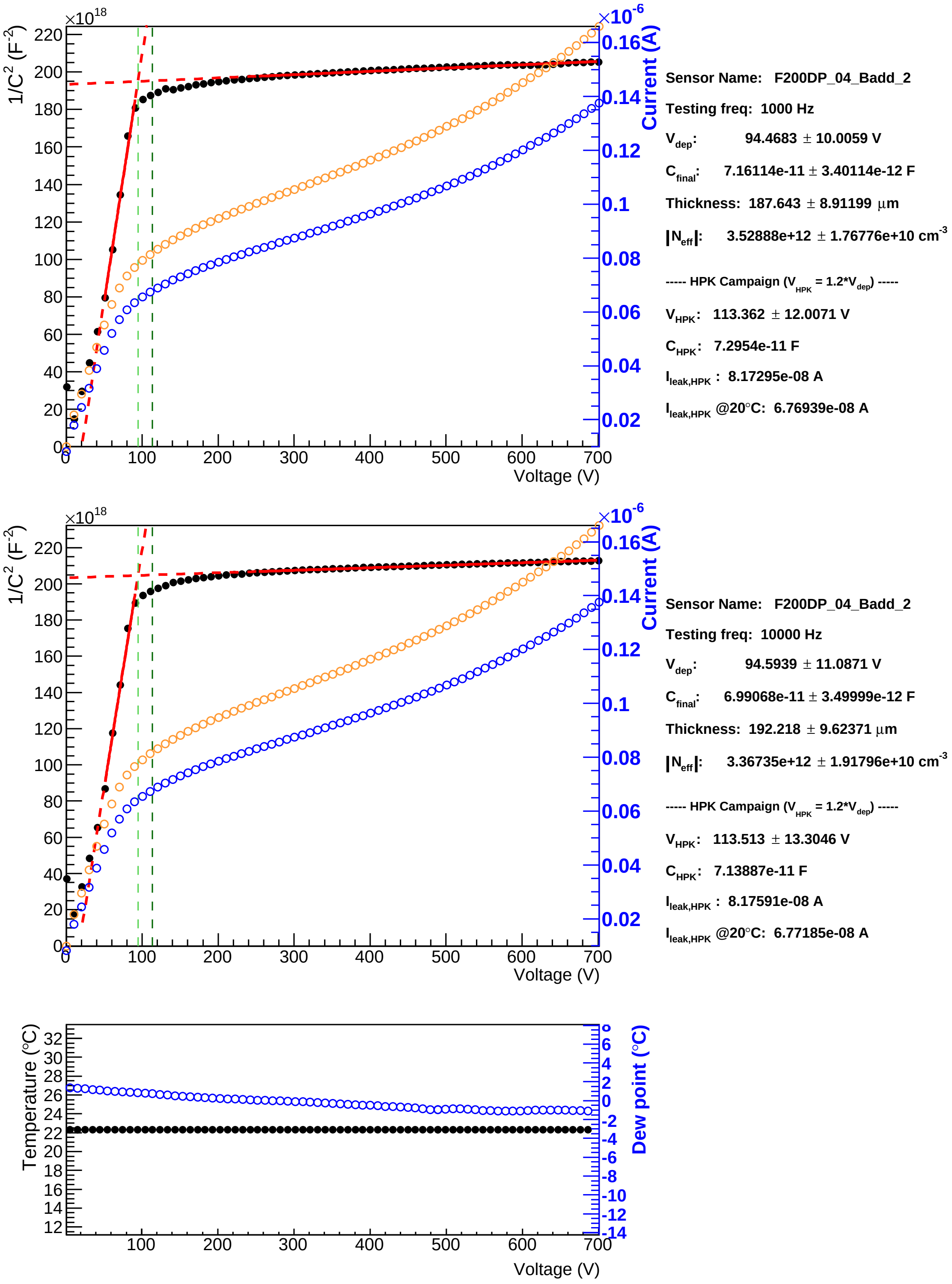

Figure 4.9: CV-IV measurements of F200DP_04_Badd_2

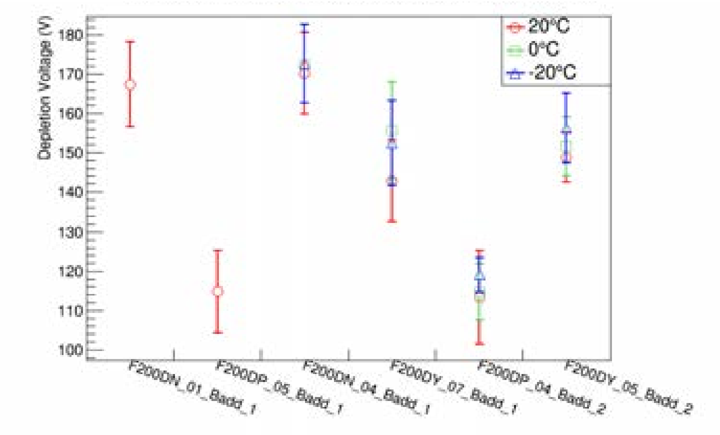

Figure 4.10: Depletion voltage of all test sensors.

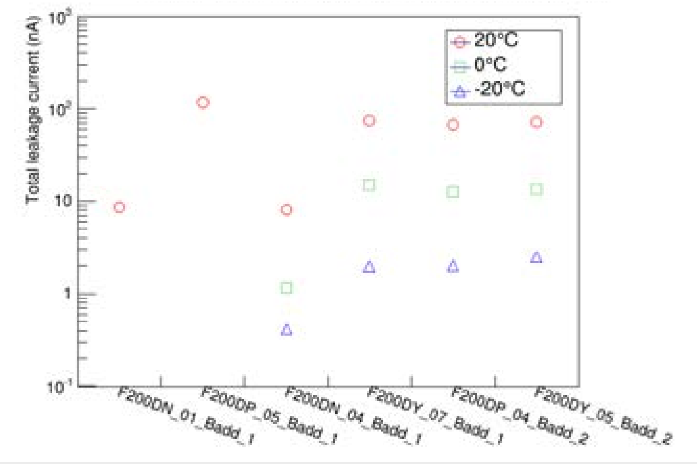

Figure 4.11: Total leakage current of all test sensors.

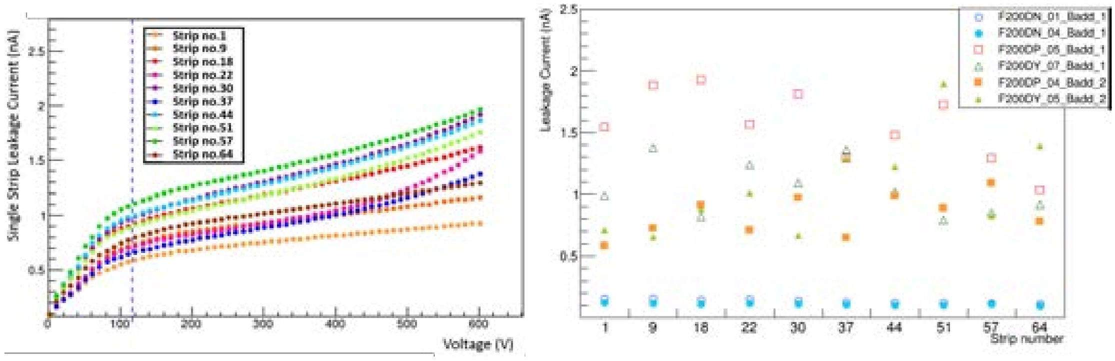

(a) (b)

Figure 4.12: Single strip leakage current of (a) F200DP_04_Badd_2 and (b) All test sensors

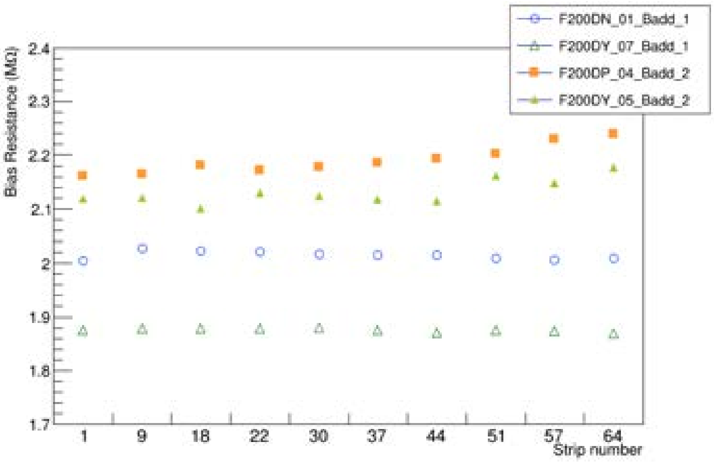

Figure 4.13: Bias resistance of all test sensors.

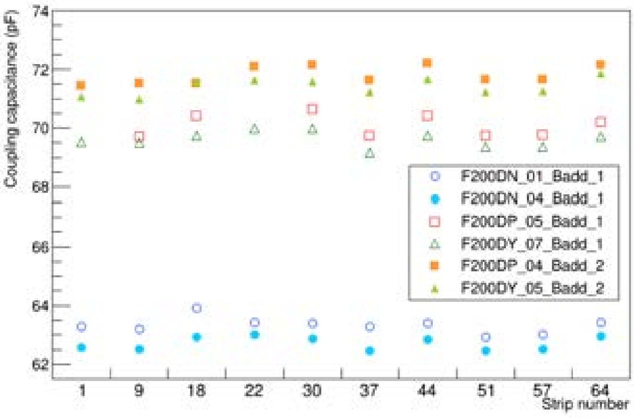

Figure 4.14: Coupling capacitance of all test sensors.

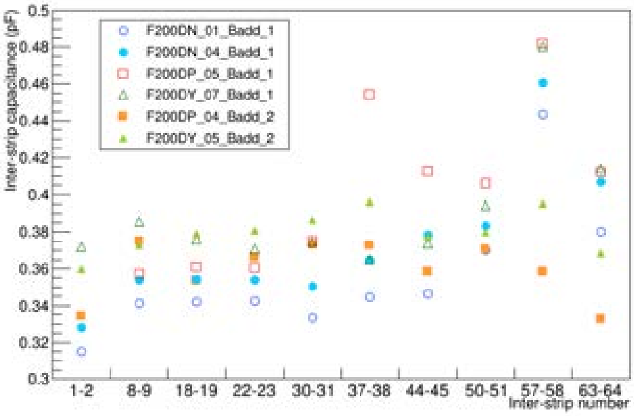

Figure 4.15: Inter-strip capacitance of all test sensors.

4.3.1 Scratches

During the measurement, mistakes happened and two of the test sensors were scratched. This results in high leakage current of the sensors (Figs. 4.16 and 4.17). Both are not used after scratched.

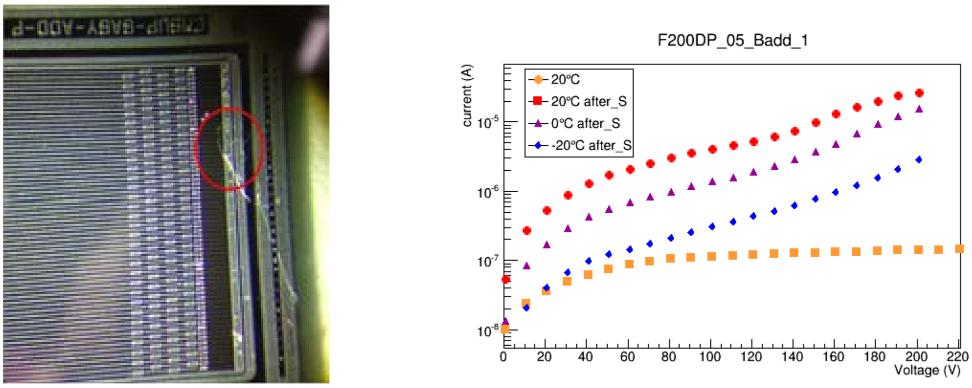

Figure 4.16: Scratch on the bias resistors and the bias ring of F200DP_05_Badd_1 sensor resulted in broken bias resistors, high leakage current on the broken strip (strip no.44-54), and high total leakage current (25 μA @200V 20°C).

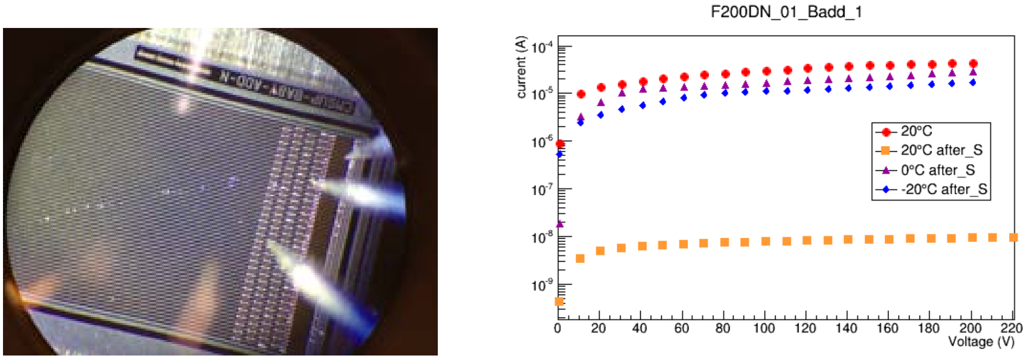

Figure 4.17: Scratch on some of the strips of F200DN_01_Badd_1 sensor resulted in pinholes between the metal routings and the implanted strips, therefore; a high total leakage current (40 μA @200V 20°C).

CHAPTER V

SIGNAL MEASUREMENTS

After the electrical characterization, two of the test sensors were bonded to the readout hybrid and were tested with signal measurement setup at Brown University. After the test, both sensors were irradiated with 800-MeV proton at the Los Alamos National Laboratory. During the shipment back to Brown University, one of the sensors was damaged. Therefore, the results after irradiation are from only one test sensor.

5.1 Setup

5.1.1 ARC setup

APV Readout Controller (ARC) system was first developed in Aachen, Germany, to provide a test environment for production and quality assurance of the CMS front end electronics and modules [14]. The ARC system at Brown University is shown in Fig. 5.1 and 5.2. The ARC system consists of ARC front end adapter and the ARC board. The ARC front end adapter is connected to the detector module through the I^2C cable. It provides the high voltage and ground connection, and amplifies the signal. The ARC board generates and distributes clock and trigger signal. Besides the ARC system, the radioactive source triggering system is included with the radioactive source holder and two photomultiplier tubes (PMTs) aligned and attached to the same moving table. The sensor is placed between the radioactive source and the PMTs. The two PMTs are used to confirm that there are particles passing through the sensor. The coincidence unit will trigger when the signal from the two PMTs arrive at the same time. This trigger is then passed on to the delay unit, then to the ARC system. The delay is needed because of the difference in processing time of the readout chip and the coincidence unit, and also because of different cable lengths. The data will be sent to the computer only when there is a trigger from the Coincidence unit. The measurement is controlled by the software developed by the team at Aachen [28]. However, the software is incomplete and we have to develop a ROOT macro to analyze the data by our own.

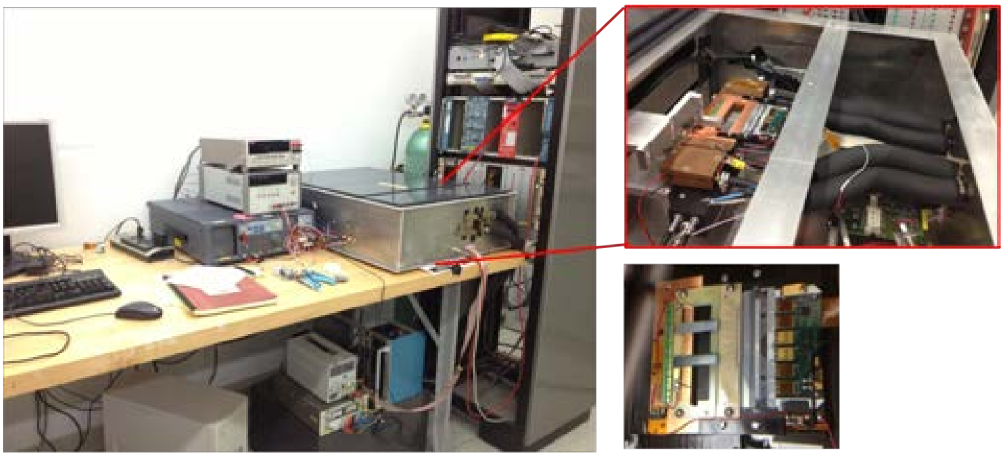

Figure 5.1: ARC setup for signal measurement at Brown University.

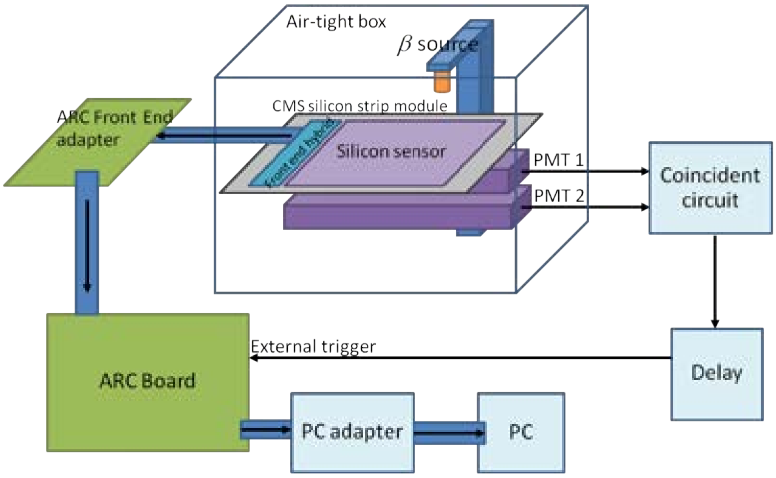

Figure 5.2: Schematic diagram of the ARC setup.

5.1.2 Module assembly

The components of the module are the test sensors, pitch adapter, readout hybrid and the supporting frames. The supporting frames were designed and made at Brown University. Then, all parts were sent to assemble at the Fermi National

Laboratory (FermiLab), USA. There are 4 APV25 readout chips on a front-end hybrid. Each chip has 128 readout channels. Two types of interface are the pitch adapter (PA) for adjusting pitches and the extender for multiple bonding (for re-using the front-end hybrid with other sensors). The wedge bonding with aluminum wire is shown in Fig. 5.3. The connection on the sensor are made at the AC-pads on the first metal layer. The finished module is shown in the upper right conner of Fig. 5.4. The following paragraphs address the problems with module assembly.

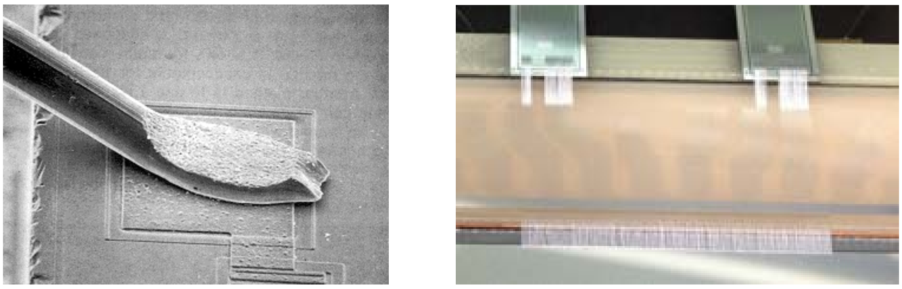

(a) (b)

Figure 5.3: Wedge bonding (a) close up[1](b) from our test sensors.

There were many problems with module assembly, which were revealed when all of the components were about to be assembled at the FermiLab. One of the planned modules and the finished module are shown in Fig. 5.4. In our case, the front-end hybrid came with a PA which adapts from 44 μm to 135 μm. The pitch of the extender is also 135 μm, while the pitch of the sensor is 80 μm. There was a misunderstanding about the pitch of the extender, therefore another PA had to be added. The extra PA was retrieved from a broken part of other sensor and did not match perfectly with our test sensors. As a result, only two test sensors were bonded to the readout electronics: F200DY_05_Badd_2 (BaddDY2) and F200DP_04_Badd_2 (BaddDP2). From all 512 channels of the readout chips, the two sensors were bonded to channel 212-255 and 340-383, respectively. A test sensor has 64 strips, but not all of the strip were boned due to the conditions of the PA. The bonding regions shown in Fig. **??** are R1: 12 strips, R2: 15 strips and R3: 17 strips. The total number of strips bonded is 44 strips per sensor.

The sensor holder was a frame made of 1-mm-thick G10 epoxy sheet (can also use ceramic plate) for electrical insulation. The base of the module is made of 0.45-cm-thick copper plate for good thermal conducting. The front-end holder are

---

[1] Figure from: http://www.ami.ac.uk/courses/topics/0268_wb/

made of PVC[2] board to seperate it from cooling region. The addition of another PA on the module required more space on the sensor holder. At that moment, the solution was to put two sensor holders on top of each other. This had later caused other problems.

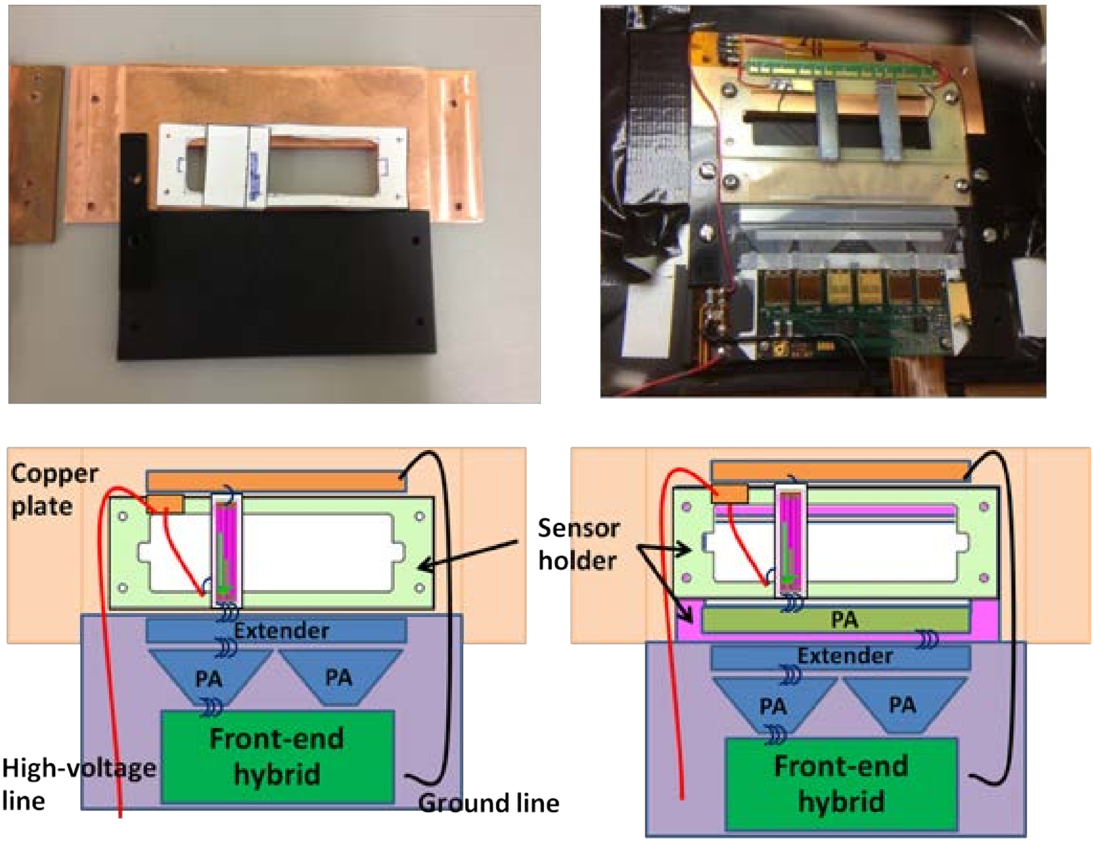

Figure 5.4: Planned module (left) and finished module (right). The two sensors on the module are: F200DY_05_Badd_2 (left) and F200DP_04_Badd_2 (right).

The module was brought back to Brown University and was tested with ARC setup. The first impression was a high current when small voltage was applied. It was found that there were shorts between the bonding wires and the edges of the sensors. This is due to the sensors' level is higher than the PA level (Fig. 5.6). The solution was to put a thin LDPE[3] plastic piece between the wires and the sensor's edge. Some bonds were broken and were then fixed by sending the module back to FermiLab.

The stacking of sensor holder also caused cooling problem. After irradiation, one sensor was broken from the shipping. The remaining one exhibited high

---

[2] Polyvinyl Chloride

[3] Low-density polyethylene

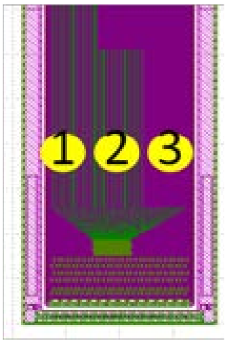

Figure 5.5: Bonding region of the test sensors.

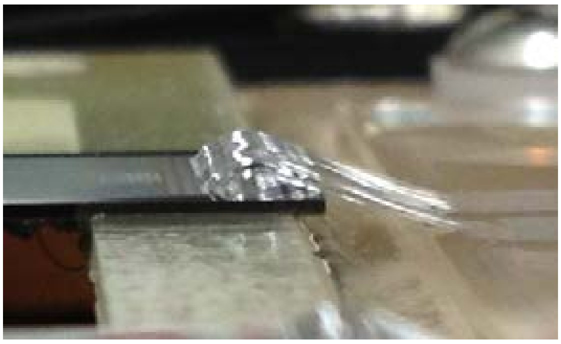

Figure 5.6: The bonding wires touch the edge of the sensor causing high current.

leakage current which was expected for irradiated sensor. The leakage current reach the limit set on the high voltage supply of 1 μA which is too high. A temperature sensor was attached to the broken sensor. It was found that the sensor could be cooled down only to $\sim$ 0°C eventhough the copper plate reached -20°C. Therefore, a small ceramic piece and nonconductive glue was inserted to the space between the copper plate and the sensor. The sensor can then be cooled down to -20°C and the measurement can then be proceeded. This part was done with the help of Alex Garabedian and David Tersegno, gradute students in the experimental particle physics laboratory at Brown University.

5.2 Measurement

Two types of measurement are made 1) without radioactive source, to find the baseline of the signal, this is know as pedestal measurement, and 2) with radioactive source, Sr90 beta source which gives high energy electrons with maximum energy of 2.2 MeV[4], this is know as signal measurement. They are described as follows:

> **Pedestal measurement** The sensor is reverse-biased at the desired voltage. Data is taken with internal trigger which is generated by the ARC board. 5,000 events were taken for each measurement. This measurement has to be taken every time before signal measurement. It describes the baseline of the signals which is highly temperature dependent.

---

[4] See Appendix B.1 for Sr90 decay chain.

Signal measurement The sensor is reverse-biased with the desired voltage. The beta source is placed over the sensor. Data is taken with an external trigger from the coincidence unit. 5,000 - 10,000 events were taken for each measurement.

Since the ARC board takes longer time to operate than external trigger from the coincidence unit, the appropriate delay must be determined before starting the experiment. This is done with the delay measurement. Then, the signal measurements are taken with varied applied voltage. This is known as the voltage ramp measurement. The descriptions of each measurement are given as follow:

Delay measurement Since the signal from the front-end hybrid is slower than the signal from the coincidence circuit, which is due to different electronic chains and different cable lengths; the delay is needed. This measurement is use to find the best dalay time for the signal from the coincidence unit, which is determined as the time that gives the highest signal. First, the dealy is set at 300 ns. Then, the pedestal measurement is taken with the applied voltage of 200V. After that, the beta source is put over one region and the signal measurement is taken at the same applied voltage. The delay time is scanned in the range of 300 - 400 ns.

Voltage ramp measurement Fig. 5.7 shows the position of the beta source over the sensor. For each region of the unirradiated sensor, the pedestal and the signal measurements were made at 20°C and -20°C[5], with the following voltages: 50, 100, 150, 200, 300, and 500 V. For the irradiated sensor, the measurements were taken at -20°C, with the same voltages as before irradiation including 600 and 700V.

These measurements were done before and after the sensor were irradiated with 800-MeV proton (see section. 3.4.1). The measurements of the sensors before irradiation were done by the author. The measurements on irradiated sensor were done by Alex Garabedian and David Tersegno.

---

[5] Due to the cooling problem, the temperature of the measurement at -20°C before irradiation should be $\sim$ 0°C.

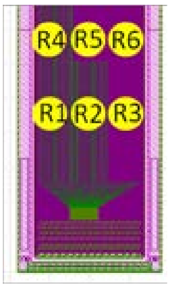

Figure 5.7: Measurement regions on the test sensor.

5.3 Signal Analysis

In each measurement, raw data from each strip are read out in ADC counts which can be converted back to the number of electrons generated in that strip[6]. The data from the pedestal and signal measurement are written into text files denoted as Pedeatal file and Signal file. ROOT macros in python were written to analyze the data. These were first developed by Alex Garabedian. In this work, I have modified the macros for analyzing new data. The analysis method is adapted from [14, 15]. The calculated parameters are:

5.3.1 Pedestal

Pedestal for i^{th} channel (PED_i) is the average output level when there is no particle signal:

$$PED_i = \frac{\sum_{n=1}^{N} RAW_i^n}{N} \tag{5.1}$$

where RAW_i^n is the raw data for n^{th} event of i^{th} channel and N is the total number of events.

5.3.2 Raw noise

Raw Noise $\left(NOI_i^{RAW}\right)$ is the standard deviation of the output level when there is no particle signal. This noise level is used to set limits for bad channels search.

$$NOI_i^{RAW} = \sqrt{\frac{\sum_{n=1}^{N} \left(RAW_i^n - PED_i\right)^2}{N-1}} \tag{5.2}$$

---

[6] See Appendix C.1

5.3.3 Common mode

Common Mode $\left(CM_g^n\right)$ is the deviation of the output from the pedestal value on an event-by-event basis that is common to a group of neighboring channels, usually the ones that are connected to the same readout chip. In our case, the strips were grouped according to its region i.e. R1, R2, R3. One can either calculate common mode using mean value or median value. The mean CM is given by:

$$CM_g^n = \frac{1}{N_{ch}} \sum_{i=g \cdot N_{ch}} \left(RAW_i^n - PED_i\right) \tag{5.3}$$

where N_{ch} is the number of channels in the same group (this is different for each test regions), g is the group number e.g. 0,1,2,... and n is the event number.

The median CM is the middle value when the RAW_i^n are sorted from minimum to maximum. In our analysis, the mean CM is found to be a little too high because the influence from the edge strips which have higher noise than the noise level of the strip in the middle of the region. Thus, the median CM is used in this analysis.

5.3.4 Signal

Signal (S_i^n) is the raw data subtracted by the pedestal and the common mode. When there is no particle signal, this value fluctuates around zero. The fluctuation is the Common mode subtracted noise.

$$S_i^n = RAW_i^n - PED_i - CM_{g(i)}^n \tag{5.4}$$

5.3.5 Common mode subtracted Noise

Common mode subtracted noise (NOI_i) is the standard deviation of the signal when there is no particle signal.

$$NOI_i = \sqrt{\frac{\sum_{n=1}^{N} \left(RAW_i^n - PED_i - CM_{g(i)}^n\right)^2}{N-1}} \tag{5.5}$$

5.3.6 Analysis steps

1) From the Pedestal file, the Pre-pedestal (PrePed) is calculated along with Raw noise used to scan for bad channels. The bad channels are defined as: noisy channel if $NOI_i^{RAW} > 3.0$ ADC and dead channel if $NOI_i^{RAW} < 0.75$ ADC. Fig. 5.8 shows the comparison between PrePed and average data from Signal file.

2) Common mode is calculated from the Pedestal file. It is then used to calculate common mode subtracted noise ($NOI_{i,PED}$). A comparison between raw noise and CM subtracted noise is shown in Fig. 5.9.

3) Pedestal (Ped) calculated from the Signal file is done by averaging the channels that do not have particle signal. By subtracting raw data from the Signal file with PrePed. The channels with particle signal are identified and excluded from pedestal calculation. Fig. 5.8 shows a comparison of the pedestal from the Pedestal file and the Signal file, and the average raw data from the Signal file.

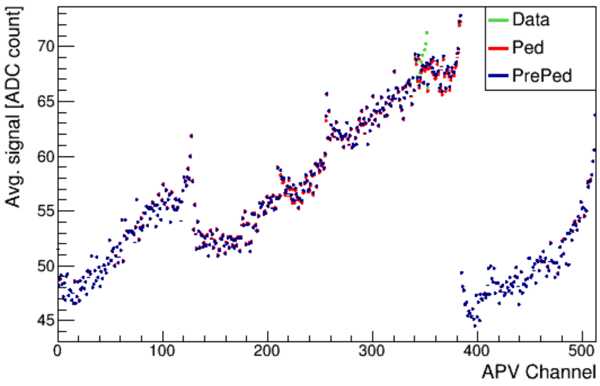

Figure 5.8: Comparison between the PrePed, Pedestal from Signal file (Ped), and the average raw data from the Signal file when the beta source is over BaddDP2 (Data).

4) Particle signal calculation in the Signal file is done as follows:

4.1) Raw data is subtracted by Ped. This is called subtracted_event.

4.2) Search for seed i.e. channel with maximum signal (max_chan).

4.3) Coarse screen: skip this event if 1) max_chan is a bad channel, 2) max_chan is an edge strip since there could be charge sharing on the edge strip (See 5)), 3) max_chan $< 2*NOI_i^{RAW}$

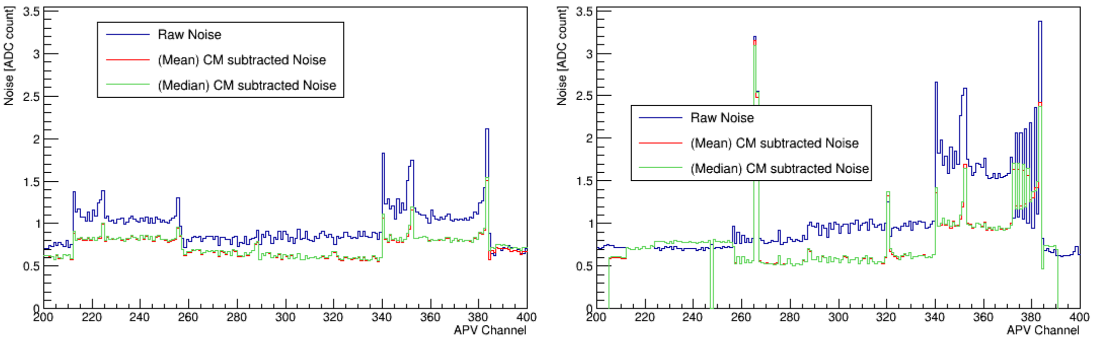

(a) (b)

Figure 5.9: Comparison between Raw noise and Common mode subtracted noise of the test sensors @300V (a) 0°C before irradiation and (b) -20°C after irradiation.

4.4) Calculate common mode (CM). Exclude max_chan and 2 consecutive strips on both side. In total, 5 strips with the chance of particle signal were excluded.

4.5) Then the signal is the subtracted_event - CM. If the signal from max_chan is less than 5*($NOI_{i,PED}$), this event is ignored. Fig. 5.10 presents signal and subtracted_event.

4.6) Start gathering signal (clustering) by looking at neighboring strips with signal > 2*($NOI_{i,PED}$). The total signal is the signals from every strip in the cluster combined. The distribution of number of strip per cluster is shown in Fig. 5.11d.

4.7) The total noise for the cluster is calculated from:
Total noise = $\sqrt{\sum_{i(cluster)} (NOI_{i,PED})^2}$

4.8) Signal to noise ratio is calculated from: (Total signal)/(Total noise)

5) The distribution of Total signal is plotted and fitted with the convolution of Landau and Gaussian function. The MPV is determined (See section 2.3.1). The contribution of signal distribution from edge strip are shown in Fig. 5.11. The small bump at low signals is from the edge strips. Therefore, edge strips are not included in searching for channel with maximum signal (4.2) and 4.3)).

6) Also the distribution for S/N is fitted with Landau function convoluted with Gaussian function, and the MPV is found.

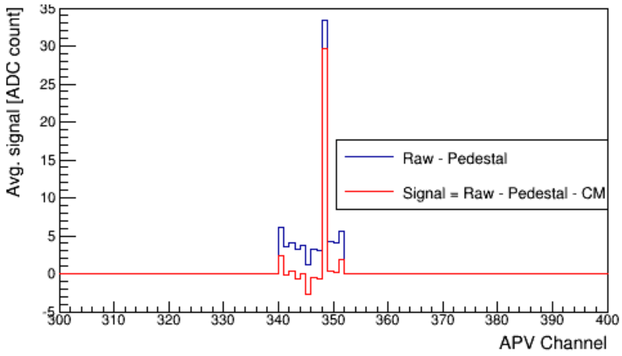

Figure 5.10: Sample signal: 1 events from R1 region @ 0°C 300V before irradiation

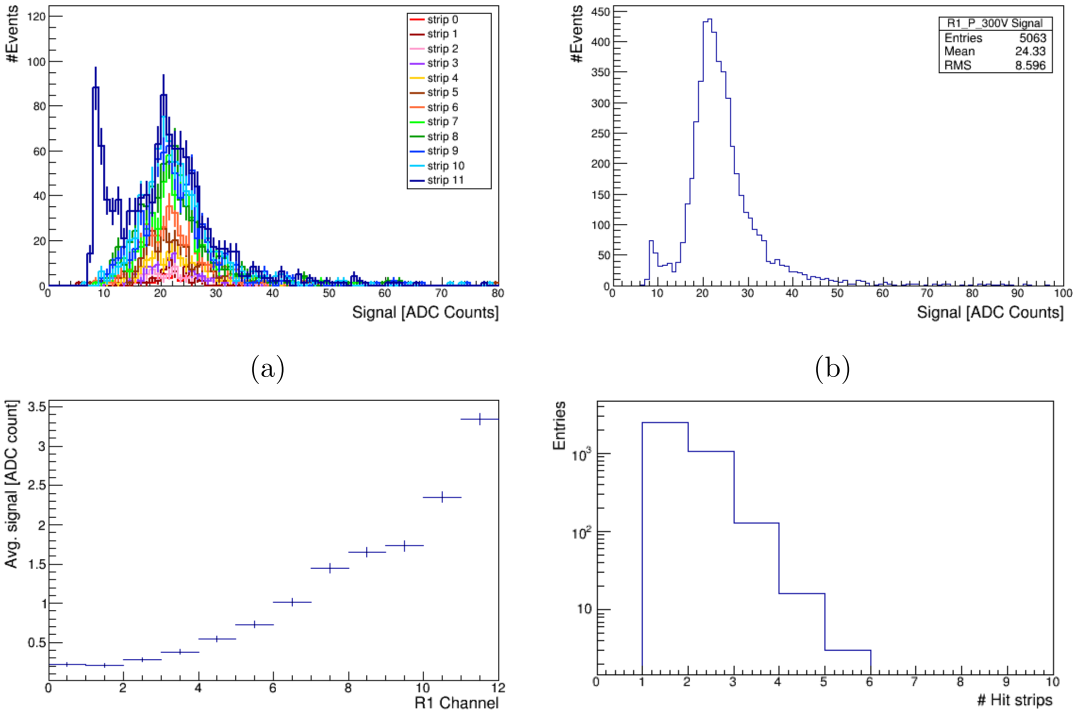

(a)

(b)

(c)

(d)

Figure 5.11: Contribution from egde strips: an example from BaddDP2 before irradiation @ 0°C 300V. (a) Signal distribution from each strip in R1, (b) signal distribution from R1, (c) average signal per channel used to tell the position of the beta source, and (d) distribution of number of strip per cluster.

The relation between MPV of signal (collected charge) and the applied voltage, and S/N are used in the further analyses.

5.4 Results and Discussion

5.4.1 Delay measurement

The MPV Vs delay of both test sensors were presented in Fig. 5.12. The delay used for both sensors in our experiment are 335 ns.

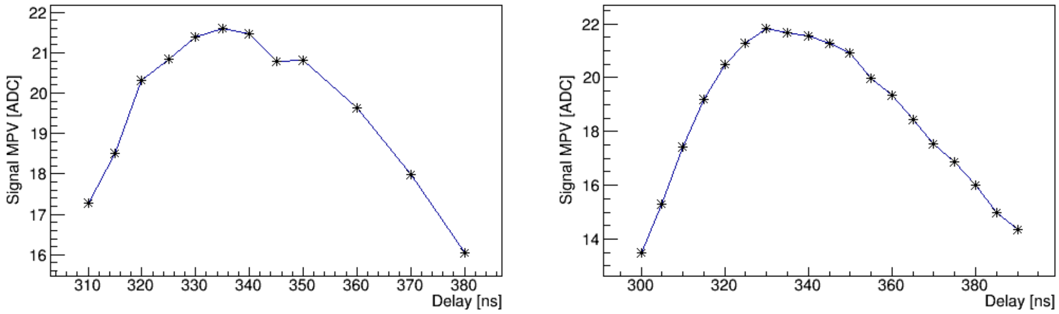

(a) (b)

Figure 5.12: Delay measurements from: (a) FZ200DP_04_Badd_2 and (b) FZ200DY_05_Badd_2

5.4.2 Voltage ramp mesurement

Charge Collection

The MPV of the total signal distribution represents the charge collected by the sensor at a specific bias voltage. The plot between charge collection and voltage can give the approximate depletion voltage. It is the voltage that give charge collection at 80% of the maximum value. The charge collection of different regions of the sensor were plotted with the separation of data from the strip with and with out double metal (DM) routing.

The charge collection of FZ200DY_05_Badd_2 before irradiation is shown in Fig. 5.13. No signifcant difference between each region is observed.

The charge collection of FZ200DP_04_Badd_2 before and after irradiation at -20°C is shown in Fig. 5.14. No significant difference between each region is observed before irradiation. The approximated depletion voltage of the irradiated sensor is ∼300V. The spread of data is seen after irradiation where R1, R2, R3 seem

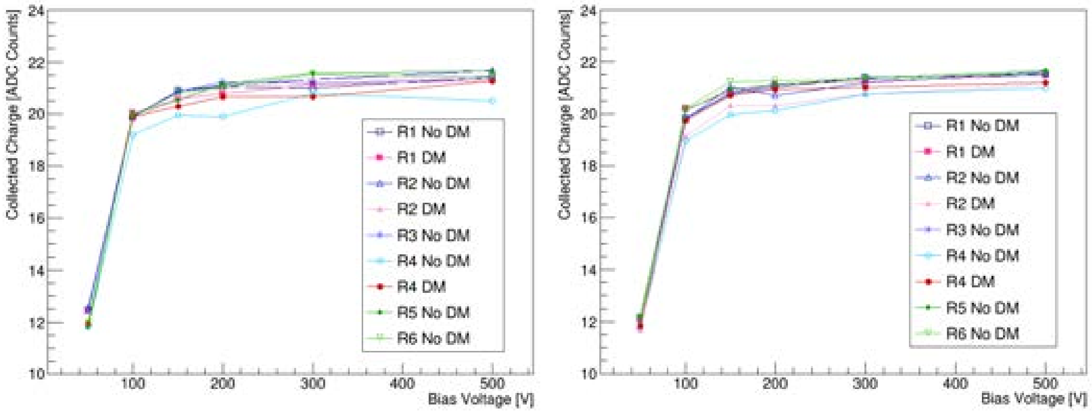

(a) (b)

Figure 5.13: Charge collection of F200DY_05_Badd_2 at (a) 20°C and (b) -20°C

to collect more charges than R4, R5, R6. The red-tone lines represent the charge collection from the strip with DM. No significant difference in charge collection between DM and no DM routing is observed.

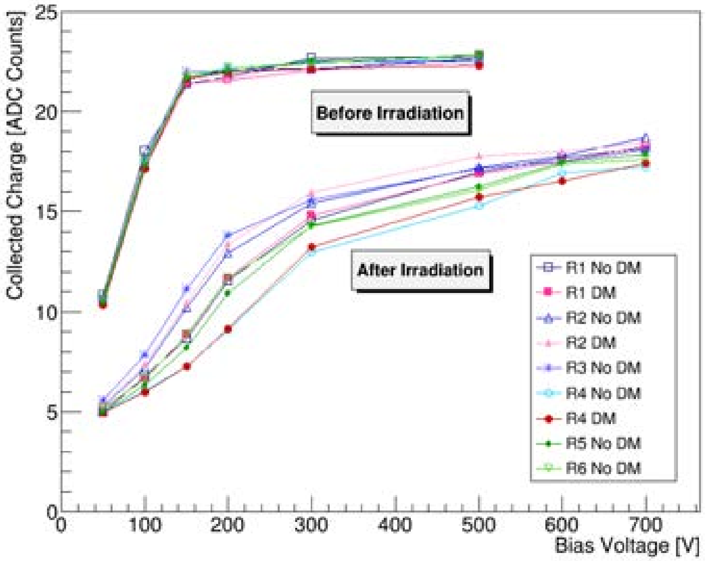

Figure 5.14: Charge collection at -20°C of F200DP_04_Badd_2 before and after irradiation

Signal to noise ratio

Signal to noise (S/N) ratio indicates the performance of sensor. The value of above 9 is preferred for sensor operation [17]. The signal to noise ratio before irradiation of F200DY_05_Badd_2 at 20°C and -20°C is shown in Fig. 5.15. No difference is seen between each region. The signal to noise ratios before and after irradiation of F200DP_04_Badd_2 at -20°C are shown in Fig. 5.16. The trend of both charge collection and S/N are the same. The S/N after irradiation is expected to be lowered because of higher noise due to defects and lower signal due to charge trapping (See section 3.4.2). Before irradiation the S/N is ∼27, while after irradiation S/N reduces to ∼17. This indicates that the sensor still works after irradiation to the proton fluence of 0.8×10^{15} cm^{-1}. No significant difference between S/N of different regions is found.

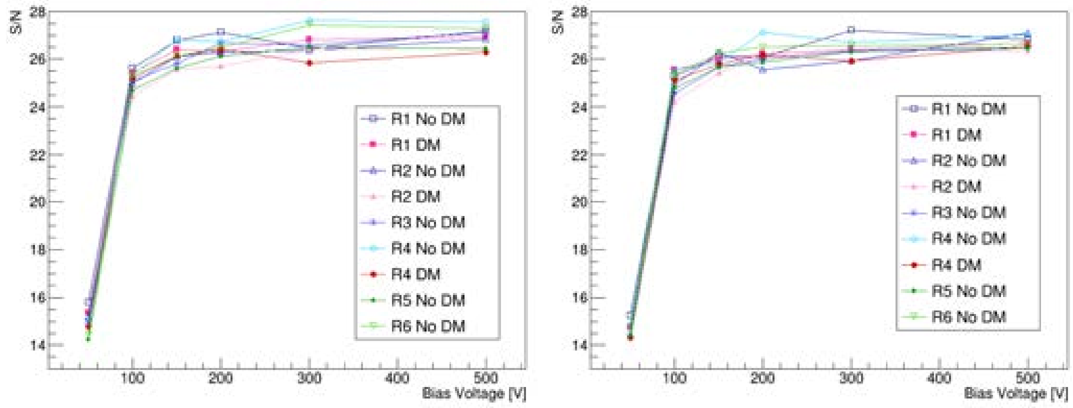

(a) (b)

Figure 5.15: Signal to noise ratio of F200DY_05_Badd_2 at (a) 20°C and (b) -20°C

Charge sharing of double metal strip

Since the Badd_2 sensor has double metal routing on every other strip. The events that have signal on at most 2 strips are further investigated for the effect of double metal routing. The charge sharing parameter η is defined as the ratio of the charge collection on double metal strip over the total charge of the cluster with 2 strips. The selection process are as follows:

1) The max_chan is selected with the condition that signal on max_chan is greater than 3*($NOI_{i,PED}$)

2) Event with 1 neighbor that the signal of neighbor > ($NOI_{i,PED}$) is marked as an event that hit 2 strips. Event with the signal of all neigbours < ($NOI_{i,PED}$) is makred as an event that hits only 1 strip

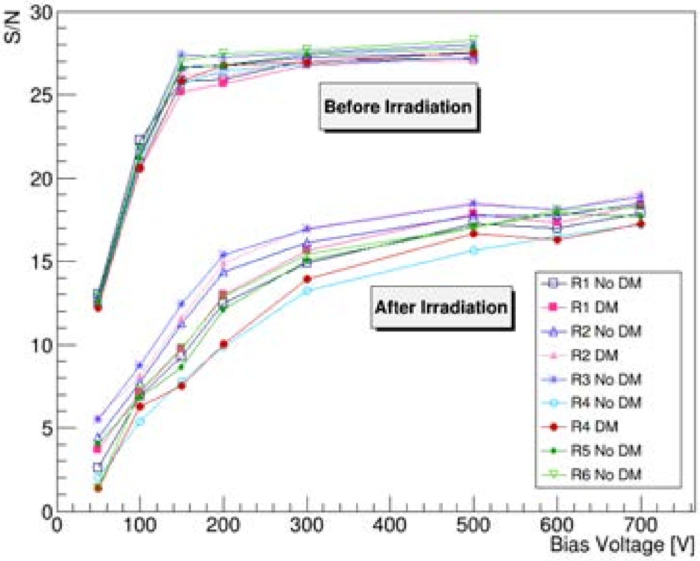

Figure 5.16: Signal to noise ratio at -20°C of F200DP_04_Badd_2

3) The total signal comes from max_chan and one other closest neighbor. By selecting the neighbor either on the right or left of max_chan that has higher signal.

4) Determine which of the two strips is double metal.

5) Find η as the ratio between 4) and 3)

6) Plot the distribution of η.

7) Normalized the distribution.

The numbers of strips in each region are ensured to be an even number. The number of hits on DM and no DM are ensured to be equal to reduce the bias from the unequal statistic. The ideal value of η is between 0 and 1 when a particle passed through only no DM strip and only DM strip, respectively. However, the neighbor can be negative if it has no signal. Therefore, the value of η can be less than 0 or more than 1. The distribution of η should be symmetric around 0.5 if every strips behave the same way i.e. no different between DM and no DM strips. It will be right skewed, if the DM strips collect lower signal than the strip without DM.

Figs. 5.17 and 5.18 show the normalized plots of η at the biased voltage higher than the depletion voltage with the mean values summarized in the graphs. The region between 0 and 1 is from charge sharing between 2 strips. Comparing between different regions, the shapes of the ditributions look the same with flat distribution between 0 and 1. The distributions look symmetric with the mean value in the range of 0.5±0.005, except for R3 and R6 after irradiation that have many bad channels and low number of events. This indicates no difference on charge sharing between strip with and without DM. Comparing before and after irradiation, the height decreasing of the two peaks and the increasing of the flat distribution's levels indicate more charge sharing. This is explained by the radiation induced defects that cause charge trapping and change of electric field in the sensor [29] (see also section 3.4.2).

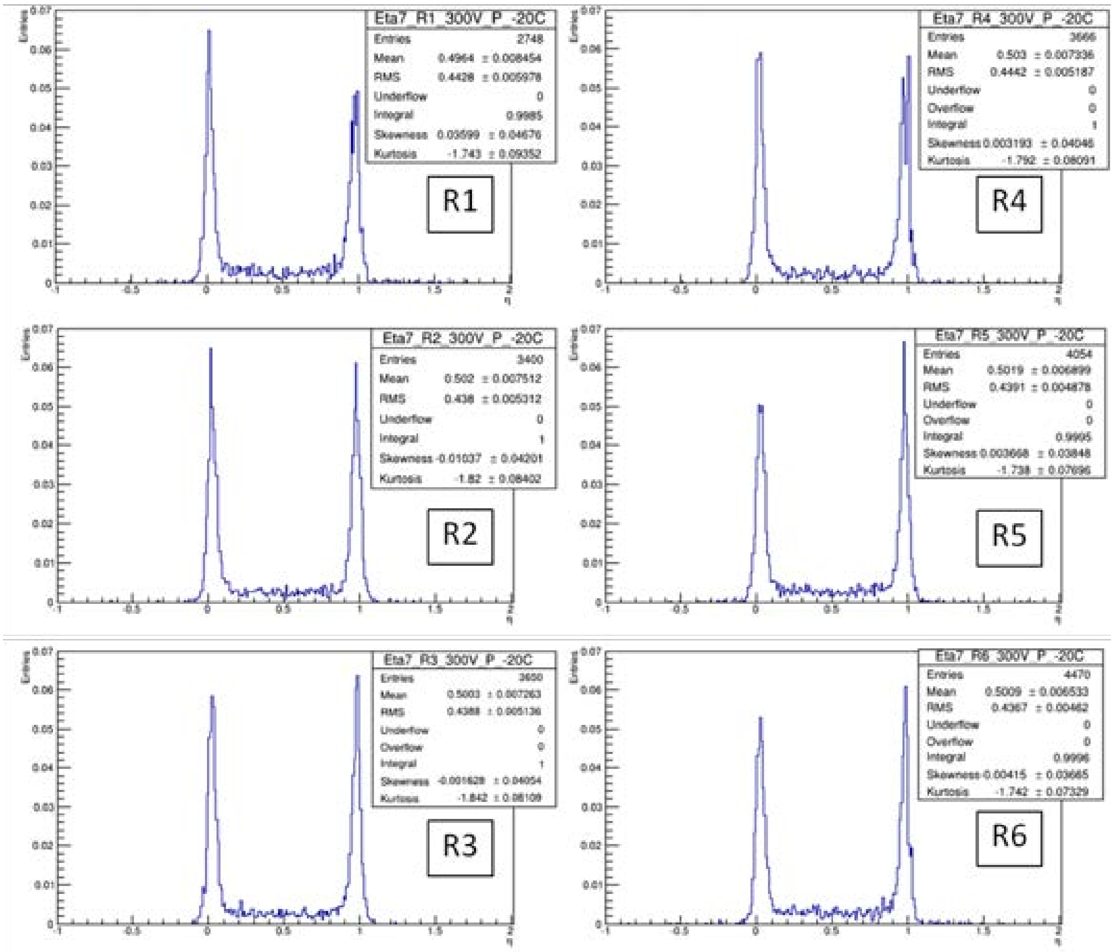

Figure 5.17: η distribution of F200DP_04_Badd_2 at 300V before irradiation.

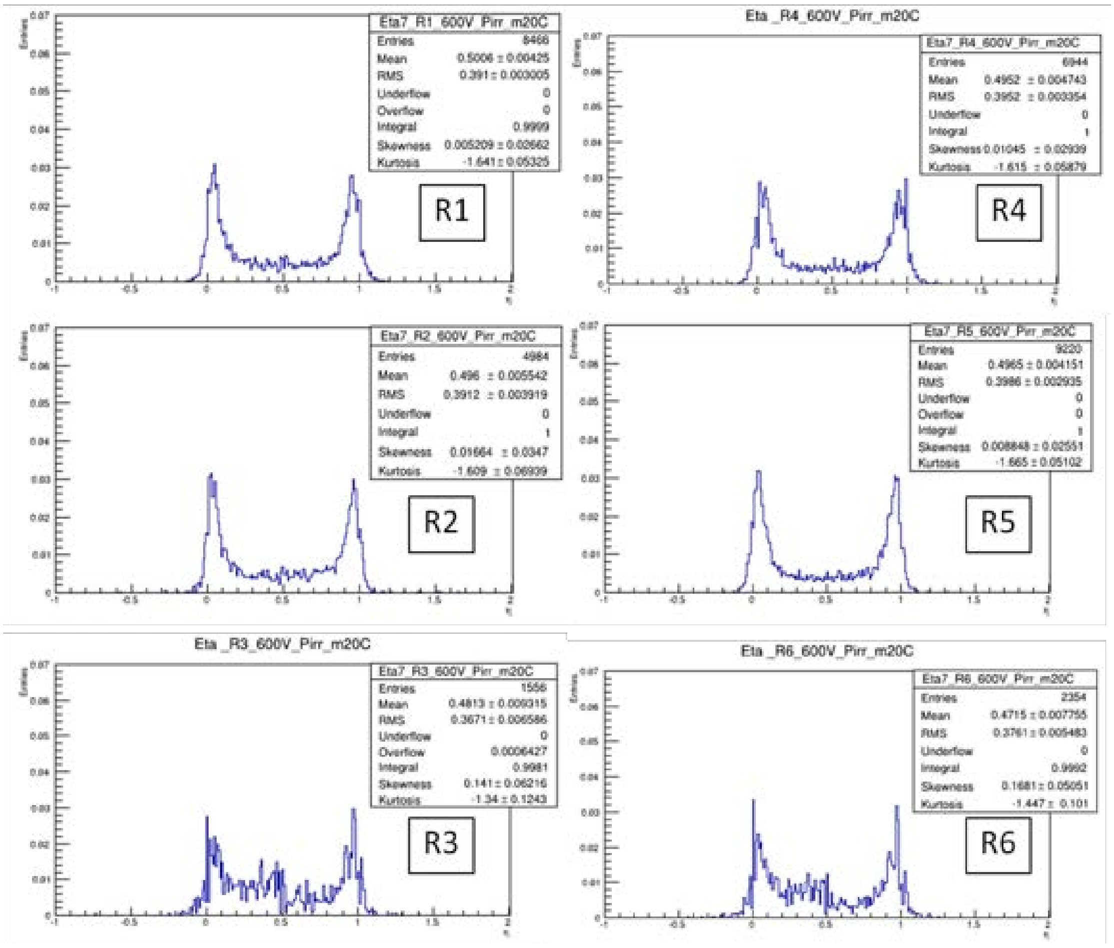

Figure 5.18: η distribution of F200DP_04_Badd_2 at 600V after irradiation.

CHAPTER VI

CONCLUSION

The test sensors in the HPK campaign with integrated pitch adapter on the second metal layer were tested for charge collection and signal to noise ratio before and after irradiation. They were characterized for electrical properties which are depletion voltage, leakage current, bias resistance, coupling capacitance, and inter-strip capacitance. All of the parameters were found to agree with the CMS specification. Two test sensors were bonded to the readout hybrid and the signal measurement were performed. After irradiation, one sensor was broken. The final results are from one test sensor that has the double metal on every other strip and has the pitch adapter which adapts from 160 to 44 μm. The depletion voltage after irradiation was approximated from the charge collection-voltage plot to be $\sim$300 V. The signal to noise ratio of greater than 10 indicated that the performance of the sensor after irradiation is still fine. The charge collection and signal to noise ratio on different regions of the sensor showed no significant difference. Further investigation was made on the events that a particle passed through at most 2 strips. Since the test structure has strips with double metal alternated with strip without double metal. The charge sharing parameter η is a ratio between the charge collection from the double metal strip to the total charge collection from the two strips. The symmetric graphs imply no difference between strip with and without double metal both before and after irradiation. The double metal routing has no effect on the charge collection and signal to noise ratio of the test sensor. Further investigation on the region with pitch adapter would confirm this conclusion.

References

[1] The CMS Collaboration. *Technical proposal for the upgrade of the CMS detector through 2020*. Technical report CMS UG-TP-1, CERN-LHCC-2011-006, 2011.

[2] The CMS Collaboration. CMS experiment at the CERN LHC, chapter 3. *Journal of Instrumentation*, Vol.3, S08004, 2008.

[3] The CMS Collaboration. CMS Software (CMSSW), in /Geometry/ TrackerCommonData/. CERN. 2013. Available from: https:// github.com/cms-sw/cmssw/blob/CMSSW_7_1_X/Geometry/ TrackerCommonData/data/Materials/tob_module.in

[4] W.R. Leo. *Techniques for Nuclear and Particle Physics Experiments: A How-to Approach*, second edition. Springer-Verlag, 1994.

[5] G.F. Knoll. *Radiation detection and measurement*, third edition. John Wiley & Sons, Inc., 2000.

[6] J. Beringer et al. (Particle Data Group), *Phys. Rev. D 86*, 010001, 2012.

[7] K. Klein. The upgrade of the CMS tracker for super-LHC. *Proceedings of science Pos(RD09)034*, 2009.

[8] E.Migliore and G. Sguazzon. *Altered scenarios of the CMS Tracker material for systematic uncertainties studies*. Technical report CMS-NOTE-2010-010, CERN, Geneva.2010. Available from: http://cds.cern.ch/record/ 1278158

[9] F. Hartmann. *Evolution of silicon sensor technology in particle physics*. Springer, Berlin Heidelberg. 2009.

[10] F. Hartmann. Review: Silicon tracking detectors in high-energy physics. *Nuclear Instruments and Methods in Physics Research A*, 666:25-46, 2012.

[11] M. Moll. *Radiation damage in silicon particle detectors - microscopic defects and macroscopic properties*. PhD thesis, Universität Hamburg, 1999.

[12] R. Brun and F. Rademakers. ROOT - An Object Oriented Data Analysis Framework, Proceedings AIHENP'96 Workshop, Lausanne, 1996. *Nuclear Instruments and Methods in Physics Research A*, 389:81-86, 1997. See also http://root.cern.ch/.

[13] H. Spieler. *Silicon detectors: basics concepts II.* Lecture note from SLUO lectures on detector techniques, October 1998. Available from:http://www-group.slac.stanford.edu/sluo/lectures/detector_lecture_files/detectorlectures_7.pdf

[14] M. Axer. *Development of a test system for the quality assurance of silicon microstrip detectors for the inner tracking system of the CMS experiment.* PhD thesis, RWTH Aachen University, 2003.

[15] R. Bremer. *Integration of the end cap TEC+ of the CMS silicon strip tracker.* Phd thesis, RWTH Aachen University, 2008.

[16] M. Friedl. *The CMS silicon strip tracker and its electronic readout.* PhD thesis, Vienna University of Technology, 2001.

[17] M. M. Angarano, et. al. Study of radiation damage and substrate resistivity effects from beam test of silicon microstrip detectors using LHC readout electronics. *Nuclear Instruments and Methods in Physics Research A*, 488:85-93, 2002.

[18] K.-H. Hoffmann et al. R&D on novel sensor routing and test structure development. *Nuclear Instruments and Methods in Physics Research A*, 628:268-271, 2011.

[19] M. Dragicevic. *The new silicon strip detectors for the CMS Tracker Upgrade.* PhD thesis, Vienna University of Technology, 2010.

[20] R. Eber. *Investigations of new sensor designs and development of an effective radiation damage model for the simulation of highly irradiated silicon particle detectors.* PhD Thesis, Karlsruhe Institute of Technology, 2013.

[21] The LHCb VELO group. *Radiation damage in the LHCb vertex locator.* CERN-LHCb-DP-2012-005. 2013. arXiv:1302.5259v1 [physics.ins-det]

[22] K.-H. Hoffmann. Campaign to identify the future CMS tracker baseline. *Nuclear Instruments and Methods in Physics Research A*, 658:30-35. 2011.

[23] A. Dierlamm. *Silicon sensor developments for the CMS Tracker upgrade*, in 9th ICPSD, Aberystwyth, 2011. JINST-7-C01110.

[24] R. Eber. *Silicon sensor developments for the CMS Tracker upgrade*, in 3th ICATPP, Milano, 2011. CMS CR-2011/219.

[25] FNAL Tracker Group. LHC fluence calculator. Online calculation available from: http://cmstrk.fnal.gov/radsim/LHC_DoseFlux_Calculator.html

[26] A. Furguri. *Qualiity assurance and irradiation studies on CMS silicon strip sensors*. PhD thesis, Universität of Karlsruhe, 2006.

[27] European Organization for Nuclear Research (CERN). *Supply of Silicon Micro-Strip Sensors for The CMS Silicon Strip Tracker (SST)*. Invitation to Tender IT-2777/EP/CMS. Technical Specification. 2000.

[28] M. Axer et al. *ARCS: A GUI for hybrid and module testing*, Technical manual version 5.01. RWTH Aachen University, 2002.

[29] D. Passeri et al. Comprehensive modeling of silicon microstrip detectors. *IEEE transcations on nuclear science*, 44(3):598- 605, 1997.

[30] M. Gupta. *Calculation of radiation length in materials*. Technical note, PH-EP-Tech-Note-2010-013, CERN, 2010.

[31] R. Ranieri et al. *TOB modules material budget review*.presentation in TOB Meeting, CERN Geneva. 2006.

APPENDICES

APPENDIX A

A.1 Glossary

Fluence (Φ) is the total number of particle (N) passing through an area (A) or an integrated flux over time with the unit of cm^{-2}. It can also be defined as the sum of particle trajectory lengths (dl) per volume (dV).

$$\Phi = \frac{N}{A} \quad \text{or} \quad \Phi = \frac{\sum dl}{dV} \tag{A.1}$$

Luminosity is a parameter related to the properties of the particle beams in a collider. It is defined as Eq. (A.2) in the unit of cm^{-2}s^{-1}. Higher luminosity means more event rate for any specific interaction.

$$L = f\frac{n_1 n_2}{4\pi\sigma_x\sigma_y} \tag{A.2}$$

where f : collision frequency (s^{-1})

n_1, n_2 : number of particle in the two bunches

σ_1, σ_2 : transverse beam profiles in the horizontal and vertical directions (in cm), and to simplify the expression it is assumed that the two bunches are identical in transverse profile

A.2 CMS Coordinate

Fig. A.1 shows the coordinates of CMS detector with respect to its position in the LHC ring and the value of pseudorapidity at different Θ.

Pseudorapidity is an approximation of the variable *rapidity* in the case of relativistic particles. Rapidity is a parameter that its differnce is invariant with respect to Lorents boosts along z-axis which is convenient for analyses of events in a collider [6]. It is defined as:

$$\eta = -\ln\left[tan\left(\frac{\theta}{2}\right)\right] \tag{A.3}$$

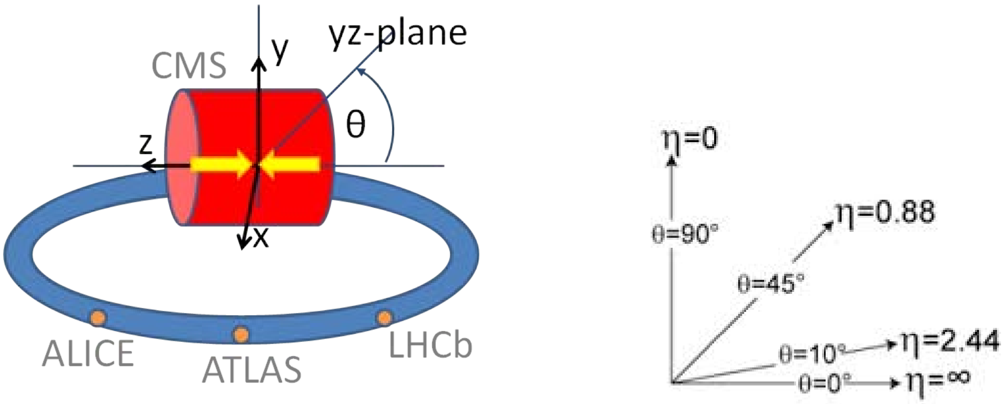

Figure A.1: CMS coordinate and pseudorapidity.

A.3 Radiation length

Radiation length, X_0, of a material is defined as (a) the mean distance over which a high-energy electron loses all but 1/e of its energy by bremsstrahlung (electron loss 64% of its energy), and (b) 7/9 of the mean free path for pair production by a high-energy photon [6]. When compare different material with different thickness (x), the ratio x/X_0 is more convenient. The radiation length can be expressed either in cm or g·cm^{-2} (cm multiplied by the density of the material).

The radiation length of elements are approximated from [30].

$$X_0 = \frac{716.4}{Z(Z+1)ln\frac{287}{\sqrt{Z}}} \quad \text{g·cm}^{-2} \tag{A.4}$$

where Z is the atomic number.

For a composite material, the radiation length can be found from:

$$\frac{W_0}{X_0} = \sum \frac{W_i}{X_i} \tag{A.5}$$

where W_0 is the total mass of the material in g.
X_0 is the radiation length of the composite material in g·cm^{-2}
W_i is the mass of individual component in g.
X_i is the radiation length of the individual component in g·cm^{-2}

A.4 Radiation length of Borosilicate glass

Borosilicate glass is a composite material. Its components are shown in table A.1.

Using Eq. (A.5), the radiation length of the borosilicate glass is calculated to be 25.214 g·cm^{-2}. With the density of the borosilicate glass of 2.51 g/cm^3, one can calculate X_0 to be 10.05 cm.

Elements	Mass fraction	Radiation length (g·cm^{-2})
Oxygen	47.52	34.24
Silicon	30.36	21.82
Potassium	5.56	17.32
Sodium	4.53	27.74
Zinc	4.50	12.43
Boron	2.45	52.63
Titanium	2.40	16.16
Aluminum	2.22	24.01
Antimony	0.46	8.725
Chromium	0.001	2.08

Table A.1: Composite of Borosilicate glass. [30, 31]

The thickness of the pitch adapters are 0.03 cm for TIB modules and 0.05 cm for TOB modules [3]. The material budget (x/X_0) for one layer of PA is then 0.003 - 0.005. In case of particle passing through all ten layers of CMS Tracker (4 layers of TIB and 6 layers of TOB, See Fig. 1.4),the overall thickness (x) will be $4 \times 0.03 + 6 \times 0.055 = 0.45$ cm. Then the maximum x/X_0 for the PA will be 0.045.

APPENDIX B

B.1 Sr90 beta source

Sr90 can deacy into Y90 with the half life of 29.12 years and maximum beta energy of 545.9 keV. Y90 can undergo beta dacay with half life of 64 hours into Zr90 with maximum beta energy of 2,284 keV (beta1) and 523 keV (beta2).

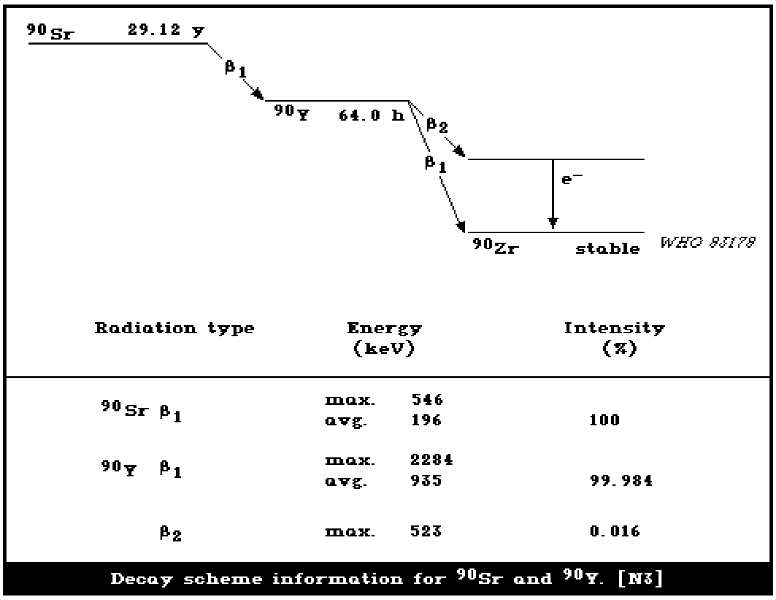

Radiation type	Energy (keV)	Intensity (%)
^{90}Sr β_1	max. 546 avg. 196	100
^{90}Y β_1	max. 2284 avg. 935	99.984
β_2	max. 523	0.016

Decay scheme information for ^{90}Sr and ^{90}Y. [N3]

Figure B.1: Decay chain of Sr90[1].

---

[1] Figure from: http://www.inchem.org/documents/ehc/ehc/ehc25.htm

APPENDIX C

C.1 Calibration

In each measurement, raw data from each strip are read out in ADC counts which can be converted back to the number of electrons generated in that strip. The calibration is the process to find this conversion factor. There are a number of ways to do the calibration. The easiest way is the internal calibration.The APV25 chip can injected a certain amount of charge into the electronics chain. From the readout ADC and the amount of charge injected, the conversion factor can be calculated. However, the ARC controlling software at Brown University cannot work on this process. Thus, we turned to the calibration using cosmic ray muons as MIPs on the CMS TOB sensor (Fig. C.1) to fitted with the energy loss from Bethe's formula. Two modules were tested. The conversion factors are 647 and 573 electrons per ADC count. However, the calibration on the test sensors were not done.

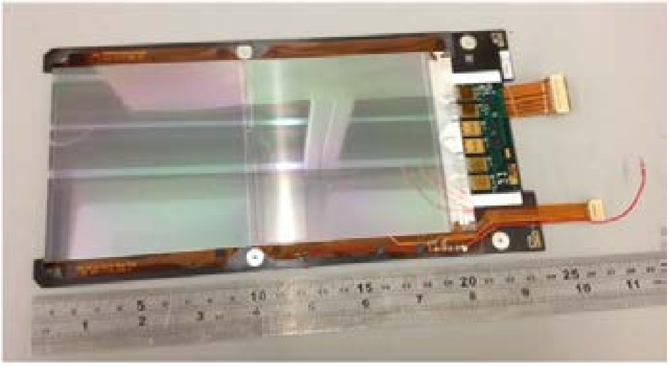

Figure C.1: CMS Tracker Outer Barrel (TOB) silicon strip module used in the attempt to calibrate the signal.

Vitae

Nanta Sophonrat was born in Khon Kaen, Thailand on the 26th of April 1989. She recieved her Bachelor's degree in physics from Khon Kaen University with the senior project in the topic of ”The calculation of forces in molecules using Hellmann-Feynmann theorem”. She has turned to work on particle physics instruments when she moved to Chulalongkorn University.

Presentation related to this work

1. Parallel Talks in the Siam Physics Congress 2014, on the topic of *Effect of a double metal layer on the performance of CMS silicon sensors: a preliminary study.* The conference was held at Rajamangala University of Technology Isan, Nakhon Ratchasima, Thailand, during 26^{th} -29^{th} March 2014.
2. Best Poster Presentation Award in The 2^{nd} ASEAN Plus Three Graduate Research Congress, on the topic of *Effect of double metal routing on charge collection of the CMS silicon strip sensor.* The conference was held by Mahidol University, Bangkok, Thailand, during 5^{th} -7^{th} February 2014.
3. Poster presentation on an internal symposium of Tokyo Metropolitan University: The global human resource program bridging across physics and chemistry, on the topic of *Effect of double metal routing on charge collection of the CMS silicon strip sensor.* The symposium was held at Department of Physics and Chemistry, Tokyo Metropolitan University, Tokyo, Japan, on 31^{th} January 2014.